PAPER O

XSP-CDP MAPPING IN COMPLEX MEDIA WITHOUT RAYTRACING

Mark A. Van Schaack

ABSTRACT

An efficient and general approach for calculating XSP-CDP mapping trajectories can be designed using the concept of wavefronts. This approach allows mapping trajectories to be calculated efficiently in complex media without raytracing. A fundamental goal of this work is to allow models obtained using combined direct and reflected arrival traveltime tomography (CDRATT) to be used to image crosswell reflection data.

INTRODUCTION

Crosswell seismic reflection imaging followed very quickly in the footsteps of VSP (vertical seismic profile) imaging technology. Wyatt and Wyatt (1981) provided the first description of how reflecting horizons could be imaged with offset VSP data. Their observation, simplified using horizontal reflectors and a 1-D velocity field, was that reflections occur from points intermediate (in offset) to the source and receiver locations. Using this simplification they described an imaging procedure, the "VSP-CDP stack", which could be used to convert time-depth seismic data to an offset-depth reflection image similar to depth migrated surface seismic sections. Soon after Dillon and Thomson (1984) published a comprehensive study of the ways the subsurface could be illuminated for a wide variety of VSP acquisitions geometries including: offset source, walkaway, and deviated well. They also used the VSP-CDP imaging approach. Almost simultaneously, Baker and Harris (1984) extended the concept of VSP-CDP imaging to include the crosswell acquisition geometry and created one of the first crosswell reflection images.

Two early papers provided a second direction to crosswell reflection imaging by introducing crosswell migration. Zhu and McMechan (1988) and Hu, McMechan, and Harris (1988) demonstrated the use of acoustic prestack finite-difference reverse-time migration on both synthetic and scale-model examples. Following these papers research in reflection imaging has been relatively evenly divided between work which advocates a mapping-based approach: Delvaux et al. (1987), Iverson (1988), Abdalla et al. (1990), Goulty et al.

(1990), Findlay et al. (1991), Smalley and Harris (1992), Lazaratos et al. (1993), and Lazaratos et al. (1995), and work performed which advocates a migration-based approach: Beydoun et al., (1989), Rowbotham and Goulty (1993), Mo and Harris (1993), Qin and Schuster (1993), and Tura et al. (1994).

While mapping-based approaches do not enjoy all the theoretical advantages of migration-based approaches they are still commonly used due to their simplicity, speed, and robustness in the presence of noise. For these reasons I have chosen to use a variation of the VSP-CDP technique to image reflections in crosswell data. To accurately map crosswell data an appropriate velocity/reflector geometry model is required. In previous work (Van Schaack, 1995a, Van Schaack, 1995b) I developed an approach for obtaining this model using Combined Direct and Reflected Arrival Traveltime Tomography (CDRATT). The results of this inversion are a 2-D velocity model and reflector geometries for selected reflection events. To image reflections in a consistent manner a mapping algorithm consistent with the model definition used in the crosswell tomography is required. I have developed a mapping algorithm that satisfies this requirement. Unfortunately, while the VSP-CDP approach is relatively straightforward it is not trivial to implement in complex models such as those obtained through a CDRATT inversion.

Typically each point on the mapping trajectory is determined separately using a ray-shooting method. This is done by linking a source and receiver pair through a reflection off a reflecting horizon. The process of linking the source and receiver requires that rays be shot one after the other with the launch angle modified slightly each time until the raypath intersects the receiver borehole closely enough to be considered "captured". When the mapping model is complex a large number of rays may be shot before the one ray needed to determine the reflection point is found. It sometimes occurs that the modifications to the launch angle become so small that the machine precision is insufficient to obtain a satisfactory raypath. In addition, even if raypaths can be determined, it can become so costly in terms of computation time as to be unfeasible.

In the first half of this paper I provide a review of the VSP-CDP transformation as applied to the imaging of crosswell seismic data. This specialized mapping algorithm is commonly referred to as the XSP-CDP transformation. Within this review I introduce a conceptual approach for defining mapping trajectories using wavefronts. I use this approach to describe how mapping trajectories are calculated in increasingly complex models. This conceptual approach is important because it is used as the basis for the fast and general mapping algorithm introduced in the next section.

In the second half of this paper I introduce a ray-theoretic technique for calculating XSP-CDP mapping trajectories without raytracing. Mapping trajectories can be calculated

quickly with this technique in 2-D velocity models with dipping and/or curved reflecting horizons. The implementation of the technique described here is designed for isotropic media but the concept can be extended easily to complex anisotropic models, including monoclinic. This algorithm reduces computation time by several orders of magnitude compared to traditional methods of trajectory calculation.

THE XSP-CDP MAPPING TRANSFORMATION: REVIEW OF BASICS

The VSP-CDP mapping algorithm, introduced by Wyatt and Wyatt (1981), is an approach which allows Offset Vertical Seismic Profile data recorded in the time-depth domain to be transformed to the offset-depth image domain. The basics of VSP-CDP mapping are applicable to the crosswell case with one important difference. One of the fundamental assumptions in VSP-CDP mapping is that each datum value in the seismic trace maps to a unique point in the offset-depth image domain. The crosswell experiment, however, allows the possibility of imaging both upgoing reflections *and* downgoing reflections so each datum value in the seismic trace maps to *two* points in the image domain. This important difference between the methods has prompted some researchers to use the designation of XSP-CDP (Crosswell Seismic Profile - Common Depth Point) mapping for the VSP-CDP mapping approach modified for the crosswell case. I will use this nomenclature in my discussion of crosswell imaging although typically upgoing and downgoing reflections are imaged in two separate steps, each similar to the VSP-CDP method.

Figure 1 provides an illustration of the XSP-CDP transformation concept. The fundamental principle of the XSP-CDP mapping technique is that each time element of a seismic trace, beginning with the direct arrival, is mapped to two potential reflection points, one pertaining to a downgoing reflection and the other to an upgoing reflection. In essence, each seismic trace is spread along the upgoing and downgoing trajectories of the corresponding source-receiver pair. A crosswell reflection image is created by mapping traces from an entire gather and imaging them simultaneously.

To illustrate the XSP-CDP mapping procedure I have computed a synthetic shot gather using a simple velocity model and reflector geometries. Figures 2 shows seismic trace data from a single source location produced in a computer simulation with a typical crosswell experiment geometry. In this simulation wells are 200 ft apart and receivers range over a 500 ft interval, 2650–3150 ft, every 2.5 ft. The source depth is 2850 ft. For simplicity the data were calculated using an acoustic finite-difference algorithm with a constant velocity model of 15,000 ft/s and horizontal reflectors defined by changes in density.

Figure 3 shows the XSP-CDP transformed seismic trace data. In this case the trace am-

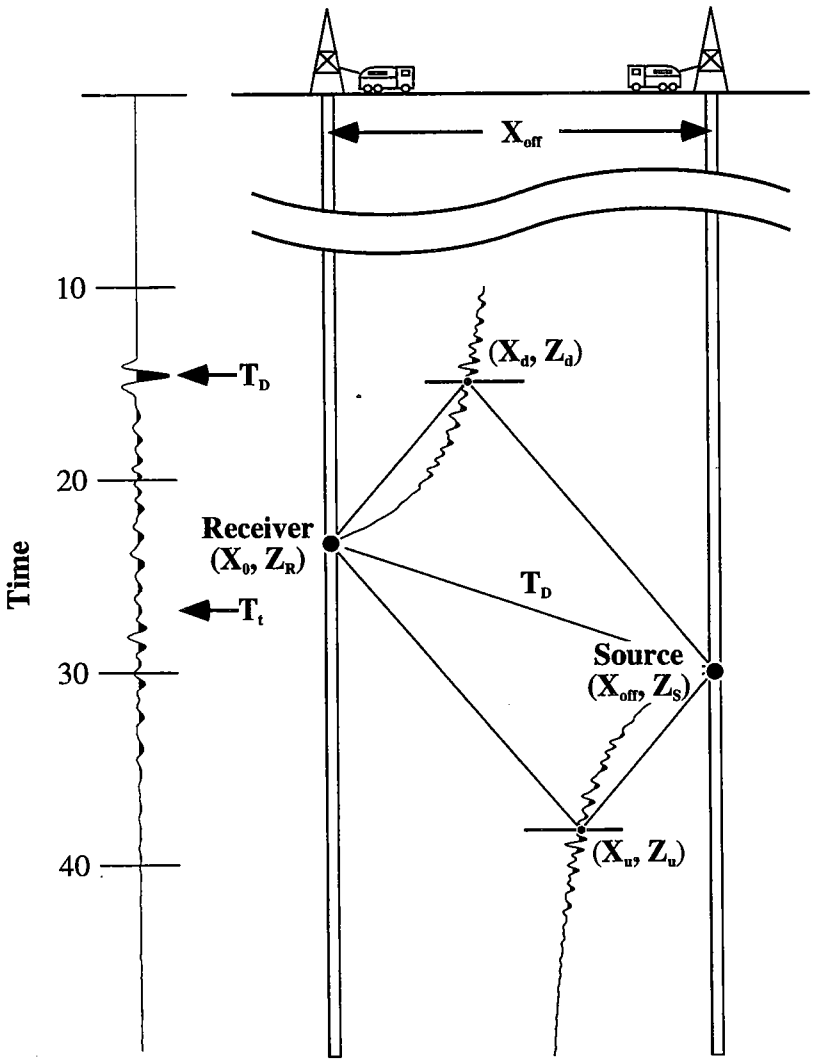

$$C = \sqrt{(T_t V)^2 - X_{off}^2} \qquad X_u = \frac{X_{off}}{2}\left(\frac{C - Z_{off}}{C}\right) \qquad X_d = \frac{X_{off}}{2}\left(\frac{C + Z_{off}}{C}\right)$$

$$Z_{off} = Z_R - Z_S \qquad Z_u = \frac{1}{2}(Z_R + Z_S + C) \qquad Z_d = \frac{1}{2}(Z_R + Z_S - C)$$

Figure 1: Basics of the XSP-CDP mapping transformation. As seen in this figure, points from the crosswell seismic trace (following the direct arrival) are mapped to two locations, one a downgoing reflection point and the other an upgoing reflection point. A mapping model, in the form of a velocity field and reflector orientations, is required to determine these points.

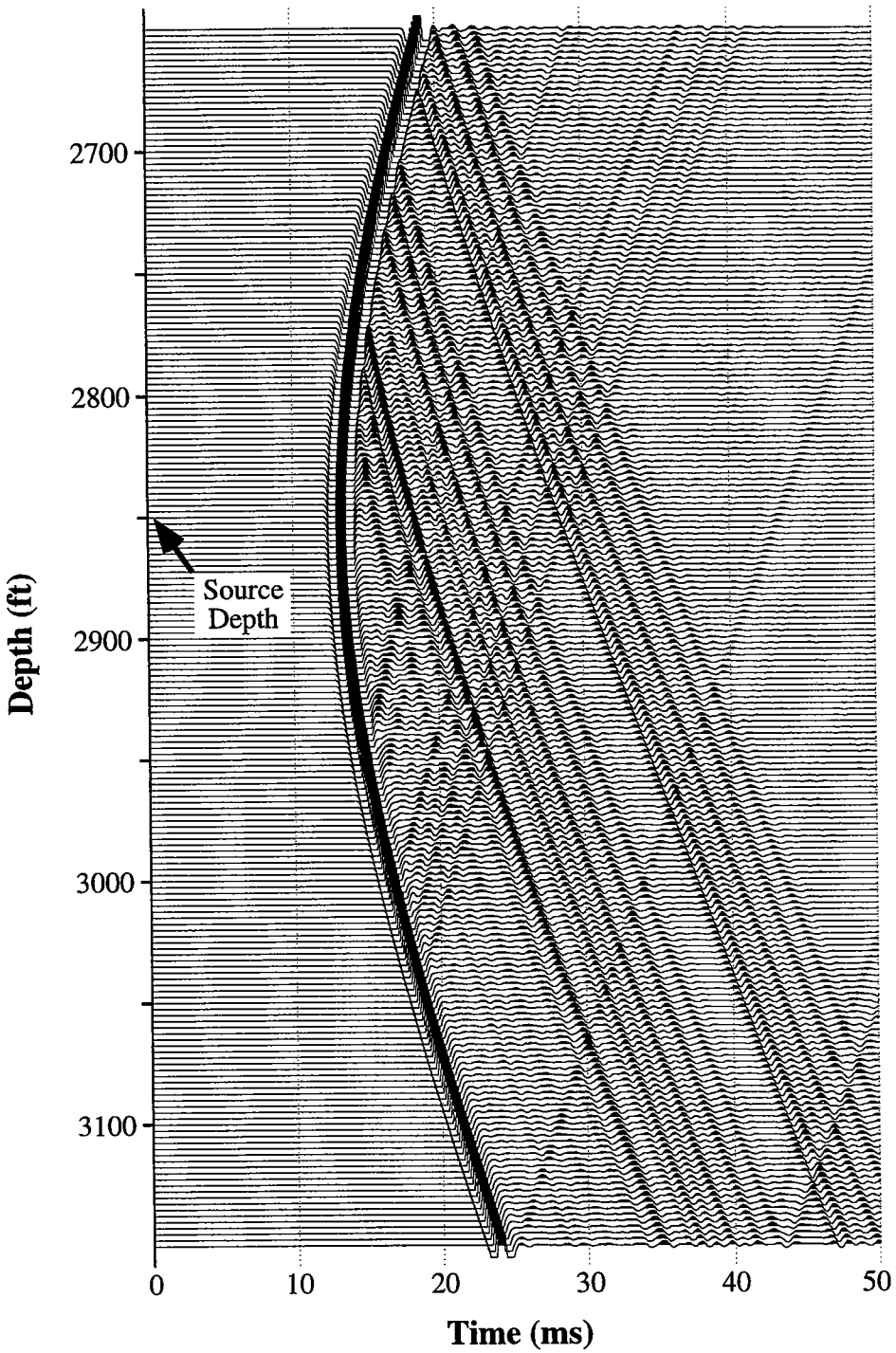

Figure 2: A crosswell shot gather simulation. The model is constant velocity, 15000 ft/s, with horizontal reflectors defined by density contrasts. The data were calculated using an acoustic finite-differences algorithm. Receiver locations range in depth from 2650–3150 ft, every 2.5 ft. The source, 200 ft offset from the receiver "well" is located at 2850 ft.

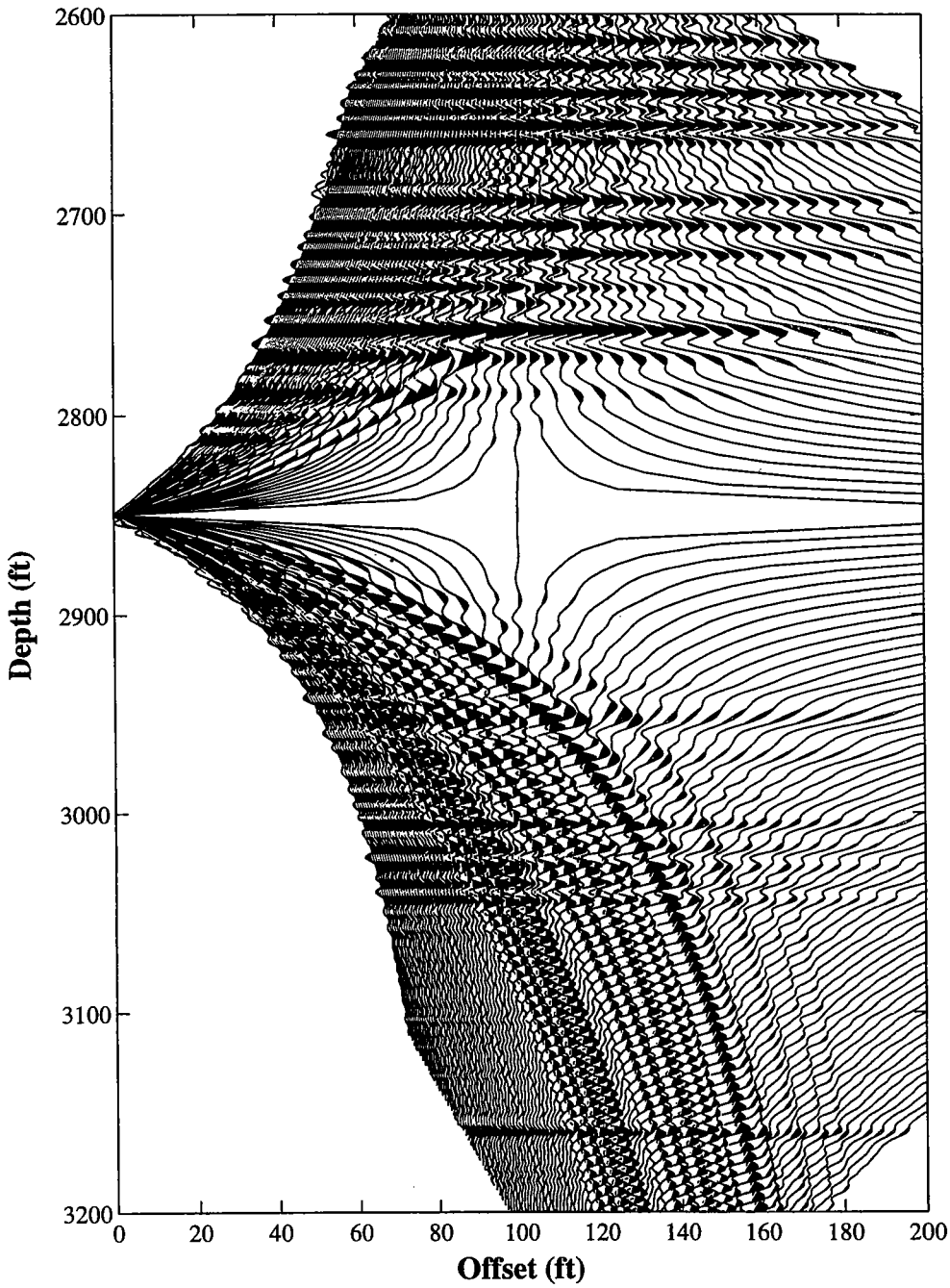

Figure 3: This is one method of displaying data mapped using the XSP-CDP transformation. The mapped data come from the shot gather simulation shown in Fig. 2. The events moving out steeply away from the source are a consequence of the XSP-CDP transformation mapping each seismic datum value to two spatial locations. The dipping events above the source are upgoing reflections imaged with the downgoing trajectories and vice versa. This illustrates the importance of upgoing/downgoing wavefield separation for optimal imaging.

plitude data have been spread over the mapping trajectories in the same manner as in Fig. 1. The data were transformed using the correct velocity and reflector information so the XSP-CDP transformation has accurately mapped events to their correct spatial locations.

While the imaging method shown in Fig. 3 is useful for illustrating the concept of the XSP-CDP transformation it is not well suited for crosswell imaging. The primary drawbacks are that images from different gathers cannot be stacked to create multi-fold images and that the mapped data cannot be post-processed in the image domain. Multi-fold imaging and post transformation filtering are crucial for optimizing signal-to-noise ratio in crosswell images (Lazaratos, 1993).

The most common method to image the transformed data is with traces evenly sampled in offset and depth. This allows images from different gathers to be stacked together directly. Resampling is typically accomplished by binning the transformed trace data and interpolating between the bins in the horizontal and vertical dimensions. Following this the interpolated data are sampled evenly to create the final seismic image. An example of this procedure applied to the gather shown in Fig. 2 is illustrated in Figure 4. I have included an upgoing and downgoing imaged trace from Fig. 3 to aid in the comparison of the two imaging techniques.

As previously described the evenly sampled image data provided by the technique shown in Fig. 4 allows stacking and processing following the mapping transformation. Another advantage of this technique is that the horizontal reflectors appear more continuous across the image, especially close to the receiver well. In the image shown in Fig. 3 the trace spacing close to the receiver well is relatively sparse making it difficult to see the reflectors. Unfortunately the results of this technique may suffer if the reflectors are not horizontal. If reflectors are dipping they may become aliased in the image domain resulting in image artifacts due to errors in the interpolation. This can be minimized by transforming the data from domains which provide more even spacing of the image domain. This is discussed in more detail later in this paper in the Examples section. In general though, Fig. 4 provides an accurate image of the mapped data and is the better choice for interpreting the reflection events.

The mapped gather shown in Fig. 4 highlights several important points about XSP-CDP imaging. 1) Unlike traditional VSP-CDP imaging the XSP-CDP transformation images reflectors below and *above* the source point. 2) Reflections outside the acquisition geometry, e.g. above 2650 ft and below 3150 ft, can be imaged. 3) Horizontal reflectors are readily apparent in Fig. 4 but so are other events curving upwards and downwards from the source location. Events curving up above the source depth are upgoing reflections and events curving down below the source depth are downgoing reflections. Since data in each trace are

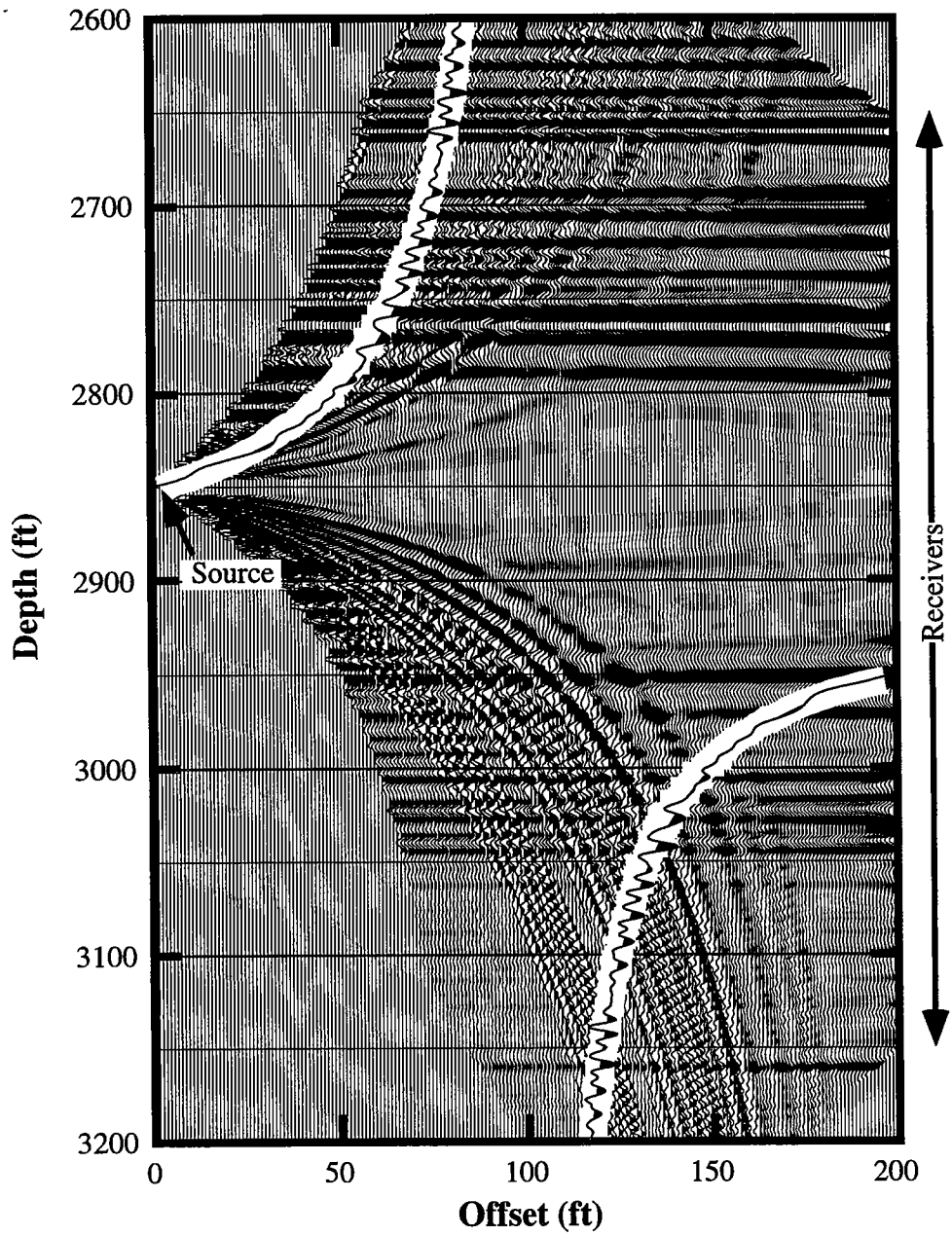

Figure 4: A crosswell shot gather simulation, from Fig. 2, mapped using a conventional imaging technique. Compare this display with that shown in Fig. 3. A trace from that display is included to aid this comparison. The primary advantage of this format is that the mapped data can be further processed before and after stacking with other mapped gathers to improve the signal-to-noise level.

mapped to two points in the XSP-CDP transformation events that map correctly in one part of the image, a downgoing event for instance, will show up as coherent noise when mapped along the trajectories calculated to map upgoing events. In other words, when imaging reflections from one direction, the reflections coming from the other direction map as noise. This illustrates the importance of wavefield separation in creating optimal images.

XSP-CDP MAPPING TRAJECTORIES IN COMPLEX MEDIA

In this section I review the concepts behind calculating mapping trajectories in increasingly complex isotropic models: 1-D velocity and reflectors, 1-D velocity and 2-D reflectors, and finally 2-D velocity and reflectors. To aid in this review I use a conceptual approach for defining reflection points which makes use of wavefronts. The value of this approach is that it serves as the basis for the mapping algorithm described later in the paper.

XSP-CDP mapping trajectories in 1-D media

The basic method for defining XSP-CDP mapping trajectories is illustrated in Figure 5. To simplify the explanation the example shown in Fig. 5 consists of a homogeneous velocity model (and therefore straight rays) and six horizontal reflectors. I will focus on the upgoing reflections and the resulting upgoing reflection mapping trajectory, the idea behind the downgoing mapping trajectory is similar. Three reflecting interfaces are responsible for upgoing reflections in Fig. 5: Horizons C, D, and E. These three horizons result in reflections from points R_C, R_D, and R_E. Horizon C lies at the same depth as the receiver so the reflection point, R_C, is located at the receiver position. Reflection points R_C and R_D lie intermediate to the two wells. Reflection points R_C, R_D, and R_E define the mapping trajectory at their corresponding depths. The complete upgoing reflection mapping trajectory is defined by the reflection points for upgoing reflections at all possible depths.

Mapping data from the seismic trace to points along the mapping trajectory requires that the traveltime from source, to each reflecting point, and on to the receiver be calculated for all points on the trajectory. This is typically done during the calculation of the mapping trajectory. Once all this information is available mapping is accomplished simply by placing the amplitude values from each time step of the seismic trace at the x-z image coordinates corresponding to the equivalent time value on the mapping trajectory. One point to be noted in this constant velocity example is that a change in velocity does not alter the x-z location of the mapping trajectories. The velocity of the medium changes only the traveltime values associated with the x-z points on the trajectories and where along the trajectory

the trace data values are placed.

Determining reflection points using wavefronts and combined traveltime maps

To more clearly show how the XSP-CDP mapping algorithm is extended to 2-D velocity models, dipping reflectors, and curved reflectors I will first describe a general approach for defining reflection points using the concepts of reciprocity, traveltime maps, and wavefronts. This approach will be used later in this paper as the basis of a method for calculating mapping trajectories without raytracing.

Figure 6 illustrates a simple source and receiver geometry with wavefronts corresponding to a constant velocity model. A source wavefront is defined by the trajectory of points which all have the property that the traveltime from the source location to any of these points is constant. Defining the receiver wavefront requires the use of reciprocity. Reciprocity states that the traveltime between two points is independent of the direction of travel. Using reciprocity the receiver wavefront can be defined in the same way as the source wavefront. The receiver wavefront consists of the trajectory of points which have the prop-

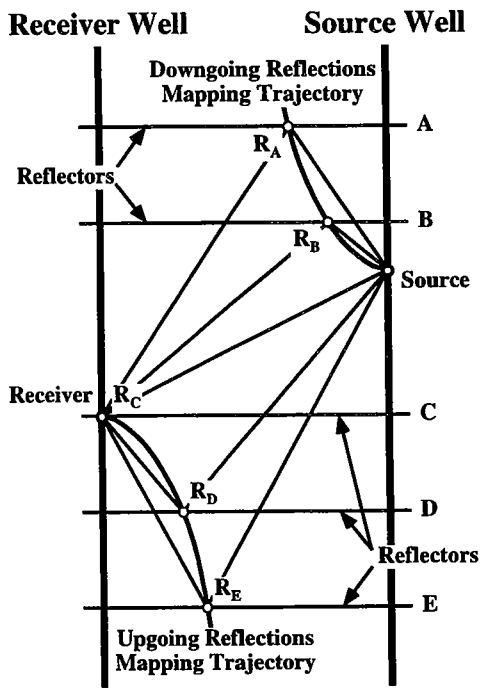

Figure 5: XSP-CDP transformation upgoing and downgoing mapping trajectories in a simple homogeneous model with flat reflectors.

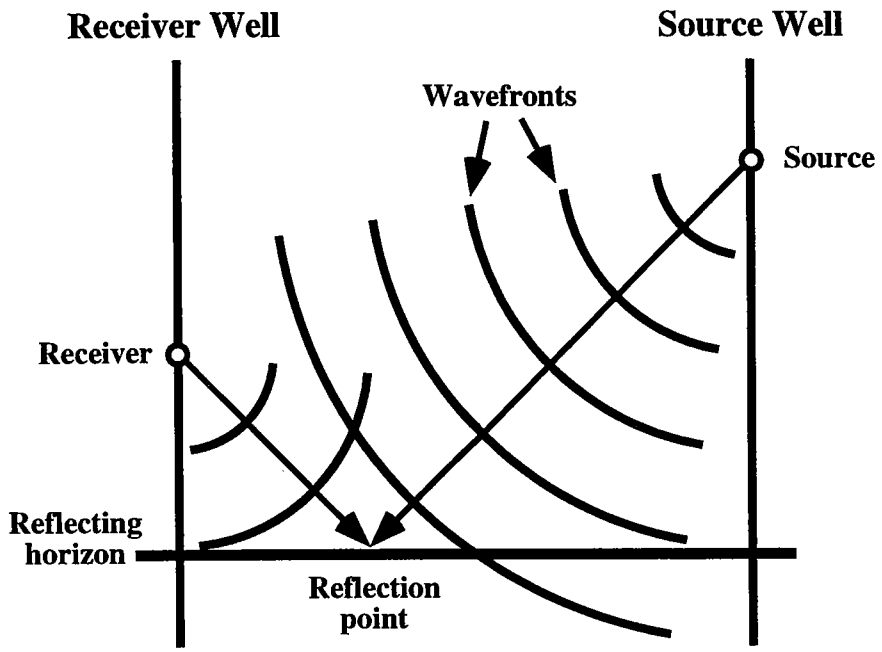

Figure 6: Source and receiver wavefronts for a simple homogeneous model. The wavefronts represent isochrons of the source and receiver traveltime maps. The raypaths, such as those shown, will always be orthogonal to the wavefronts.

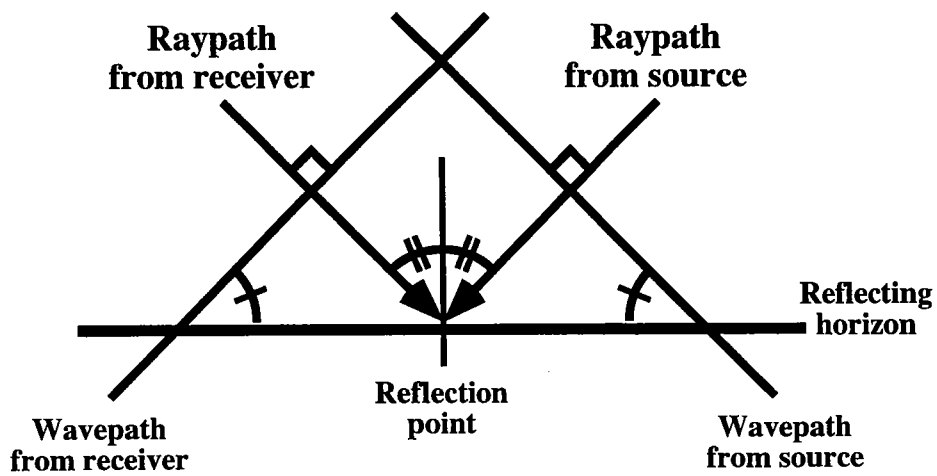

Figure 7: The reflection point of Fig. 6 shown at the limit of small scale. At this scale the source an receiver wavefronts can be approximated by lines. A consequence of the Law of Reflection in terms of wavefronts is that the source and receiver wavefronts, along with the reflecting horizon, make up the sides of an isosceles triangle at the reflection point.

erty that the traveltime from the receiver location to any of these points is constant.

Figure 7 shows the reflection point of Fig. 6 at the limit of small scale where the source and receiver wavefronts can be approximated by lines. The Law of Reflection states that the incident angle to the reflected point equals the reflected angle. The incident angle of the source wavefront can be defined using the normal to the wavefront at the reflection point. Reciprocity allows the direction of travel of the reflected wave to be reversed so that the normal to the receiver wavefront at the reflection point is equivalent to the direction of travel of the reflected wave. In Fig. 7 it can be observed that a consequence of the Law of Reflection in terms of wavefronts is that the source wavefront, the receiver wavefront, and the reflecting horizon make up an isosceles triangle at the reflection point. From this observation the Law of Reflection can be restated using wavefronts as: the angle between a wavefront from a source point and a reflection surface is equal to the angle between a wavefront from the receiver point and the reflection surface (Matsuoka and Ezaka, 1992).

The next step in describing this general approach for determining reflection points is to define the combined traveltime map and the properties of its isochrons. First it is necessary to describe source and receiver traveltime maps and their wavefronts. A source traveltime map is an image where the value of each x-z point on the map equals the traveltime from the source location to that point. Based on this definition the source wavefronts are defined by isochrons on the source traveltime map. A receiver traveltime map is equivalent to the source traveltime map except the values of the map equal the traveltimes from the receiver location to every point on the map.

The combined traveltime map is simply the sum of the source and receiver traveltime maps. Figure 8 shows a schematic illustrating the addition of source and receiver traveltime maps to create the combined traveltime map. A constant velocity model is used in this example which results in circular wavefronts/isochrons in the source and receiver maps and elliptical isochrons on the combined traveltime map. One important feature of the isochrons of the combined traveltime map is that at any point on the isochron the angle between the source wavefront and the tangent to the isochron equals the angle between the receiver wavefront and tangent to the isochron. This feature, combined with the Law of Reflection for wavefronts, means that *a reflection point on an arbitrarily defined reflecting horizon is located where the tangent of the combined traveltime isochron equals the tangent of the reflecting horizon.*

Therefore, a conceptually easy approach for calculating reflection points for source-receiver and reflecting horizon pairs is to first calculate isochron ellipses on the combined traveltime map for all traveltimes. The next step is to find points where the tangent of an isochron equals the tangent of the reflecting horizon under consideration. The x-z point of

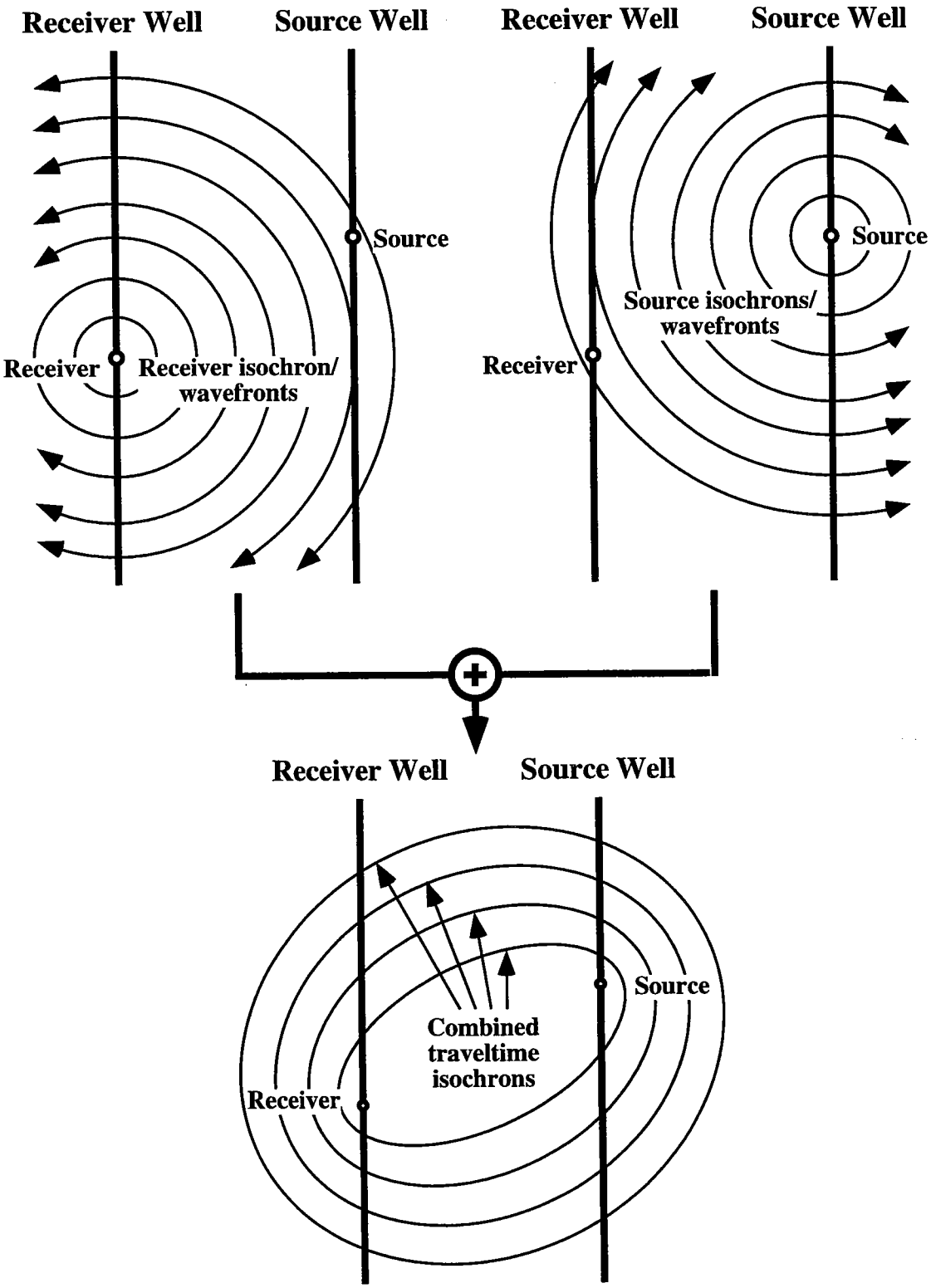

Figure 8: A schematic illustrating the source and receiver traveltime maps being added to create the combined traveltime map.

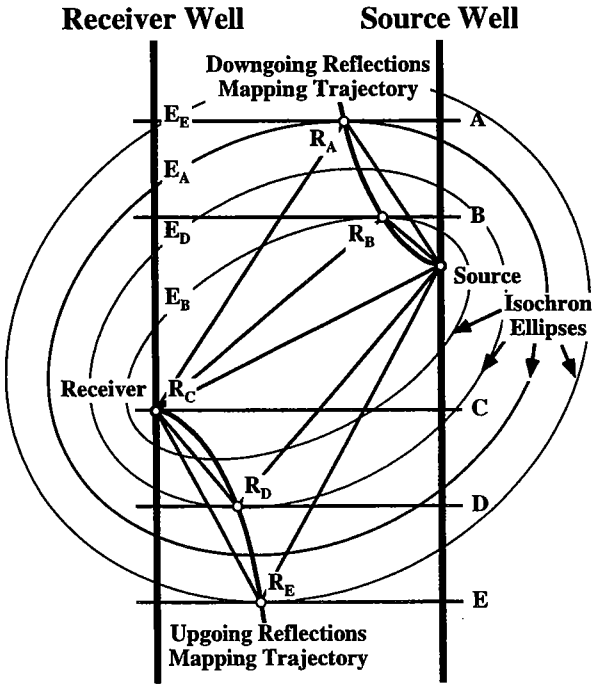

Figure 9: The mapping trajectories shown in Fig. 5 formulated in terms of shared points of tangency between the reflecting horizons and isochrons of the combined traveltime map.

tangency is the reflection point and constitutes a point on the mapping trajectory. One potential source of ambiguity is where there is more than one point of tangency between the reflecting horizon and the isochron ellipse. This however violates the assumption made in XSP-CDP mapping that there is at most one reflection point for each source-receiver-reflector combination.

Figure 9 shows the model presented in Fig. 5 with the addition of combined traveltime isochrons. Only isochrons which share points of tangency with the reflecting horizons have been plotted. Also, since the model is homogeneous the isochrons are ellipses. In this figure it can be seen how the reflection points R_A, R_B, R_D, and R_E are defined by shared points of tangency between the reflecting horizons and the combined traveltime ellipses. The combined traveltime isochron corresponding to reflection point R_C has collapsed to the line connecting the source and receiver. In the limit of this collapse the shared point of tangency lies at the receiver location.

XSP-CDP mapping trajectories with dipping reflectors

It is conceptually simple to define XSP-CDP mapping trajectories with dipping and/ curved reflector using the approach of wavefronts and combined traveltime maps to deter-

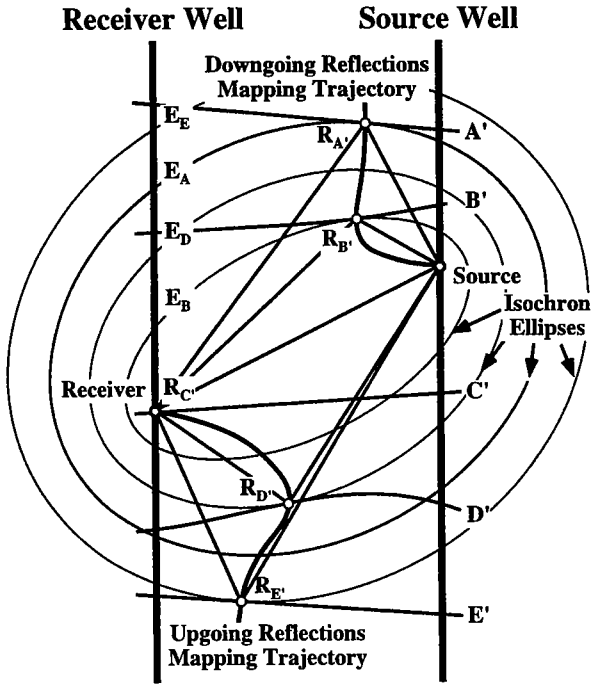

Figure 10: The wavefront method used to obtain mapping trajectories in a homogeneous model with dipping and curved reflectors. The reflection points are still defined by shared points of tangency.

mine reflection points. In Figure 10 I've modified the previous model by replacing reflectors A, B, C, D, and E with curved or dipping reflectors A', B', C', D', and E' and by updating the mapping trajectories to honor the new reflection points $R_{A'}$, $R_{B'}$, $R_{C'}$, $R_{D'}$, and $R_{E'}$. In the XSP-CDP transformation each time data value from the seismic trace is mapped to one offset-depth point for downgoing reflections and one offset-depth point for upgoing reflections. While the combined traveltime isochrons are the same as those used in the previous example the new reflectors result in new spatial coordinates for each time data value (except for reflection point $R_{C'}$). The difference in reflection locations illustrates the kind of positioning errors which can result if XSP-CDP mapping is performed with incorrect reflector geometry information. Also, in this example I've interpolated the mapping trajectory between known reflection points in a smooth fashion. The exact trajectory, however, will depend on how the reflector geometries are interpolated between known reflecting horizons.

XSP-CDP mapping trajectories in a 2-D model

The extension of the XSP-CDP mapping to accommodate 2-D variations in the velocity

field is also simple in concept using wavefronts and combined traveltime maps. The approach of finding reflection points by locating common points of tangency between the isochrons of the combined traveltime map and the reflecting horizons remains valid even though the combined traveltime isochrons are distorted by the 2-D velocity field and the raypaths are no longer straight. The ability to calculate mapping trajectories in a 2-D velocity field with 2-D reflector geometries is central to the theme of this paper. Therefore, to provide an early introduction to the kind of data used later in the field examples, I have used field data to illustrate this example. The XSP-CDP input parameters are a 2-D velocity field calculated using traveltime tomography and reflector geometries estimated from well log correlations.

Figure 11 shows the velocity model and reflector geometries. The velocity model, Figure 11a, has a velocity distribution which is primarily 1-D in nature although there are some small lateral variations. The reflector geometry model, Figure 11b, contains linear reflectors dipping slightly to the right above 3050 ft, and more steeply to the left below 3050 ft.

Source and receiver traveltime maps are calculated using a finite-differences eikonal code. Isochrons of these traveltime maps can be displayed easily using a random colortable. As this is a useful display technique I will show a specific example. Figure 12a shows a source traveltime map displayed with a conventional colortable. This map was calculated with the velocity field shown in Fig. 12a using a finite-differences eikonal code. In Figure 12b I show the same traveltime map redisplayed with a random colortable. The randomized

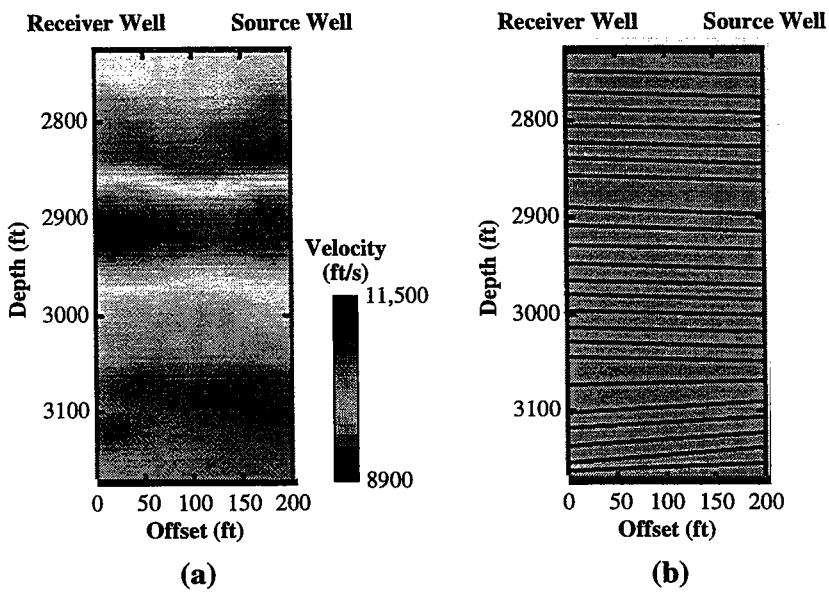

Figure 11: A 2-D velocity model (a), and reflector geometries (b), obtained from a field data experiment. These are used to illustrate the wavefront method's use for calculating mapping trajectories in general 2-D models.

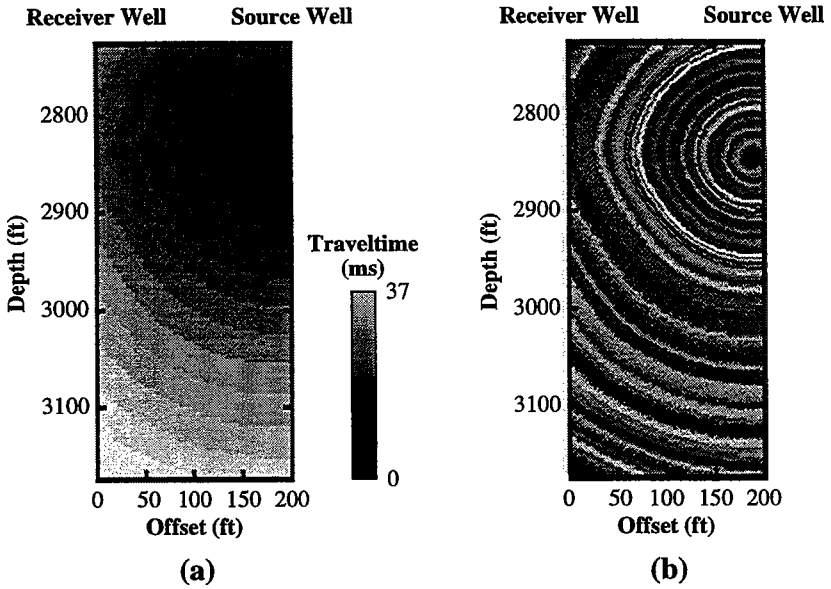

Figure 12: A source traveltime map (a) calculated from the model shown in Fig. 11 using a finite-differences eikonal code. The map is redisplayed using a random colortable in (b) to enhance the isochrons. The 2-D nature of the velocity model can be seen in the deviations of each isochron from a circular trajectory.

colortable enhances the visualization of the wavefronts of the traveltime map making it very easy to view them in a qualitative fashion.

The first step to calculating the combined traveltime map for a particular source-receiver pair is to calculate two traveltime maps, one for the source and one for the receiver. These two traveltime maps are then added together, as in Fig. 8, to create the combined traveltime map. Figure 13 illustrates this process for source and receiver traveltime maps calculated using the tomogram velocity field from Fig. 11. The traveltime maps shown in Fig. 13 are displayed with a random colortable. Paths of equal traveltime (the isochrons) are distinctive in this display. Note that the combined traveltime isochrons shapes are still relatively elliptical.

Now that I have a qualitative display of the isochron ellipsoids I can use it, along with the reflector geometries shown in Fig. 11b to determine the mapping trajectories. Figure 14 shows the combined traveltime isochron map, the reflector geometries, and the mapping trajectories in one display. The reflection points, seen at the intersections of the mapping trajectory and the reflecting horizons, are defined by points of tangency between the isochron ellipsoids and the reflecting horizons. In this example the points of tangency have been determined visually.

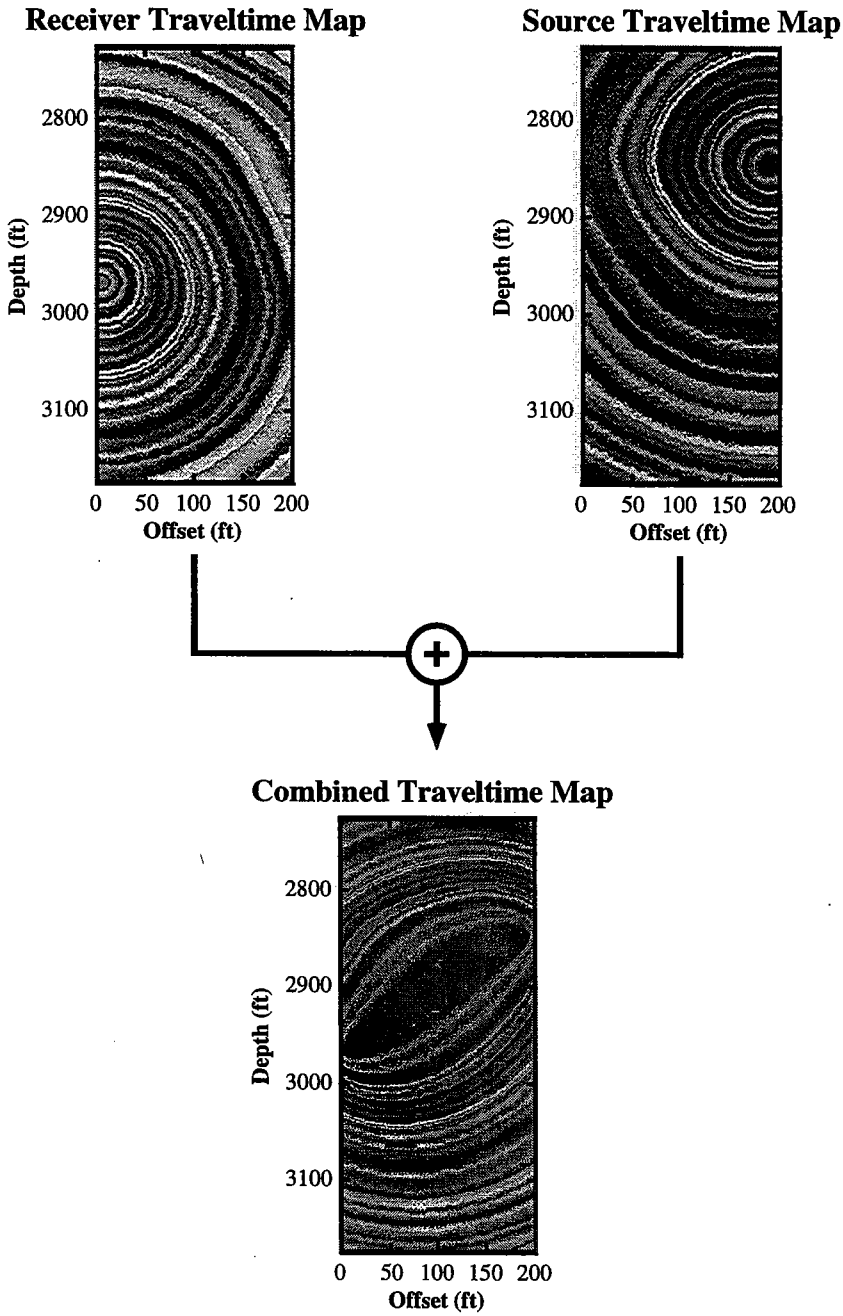

Figure 13: This figure illustrates the addition of source and receiver traveltime maps to create a combined traveltime map. The source and receiver maps were calculated using the 2-D velocity model shown in Fig. 11.

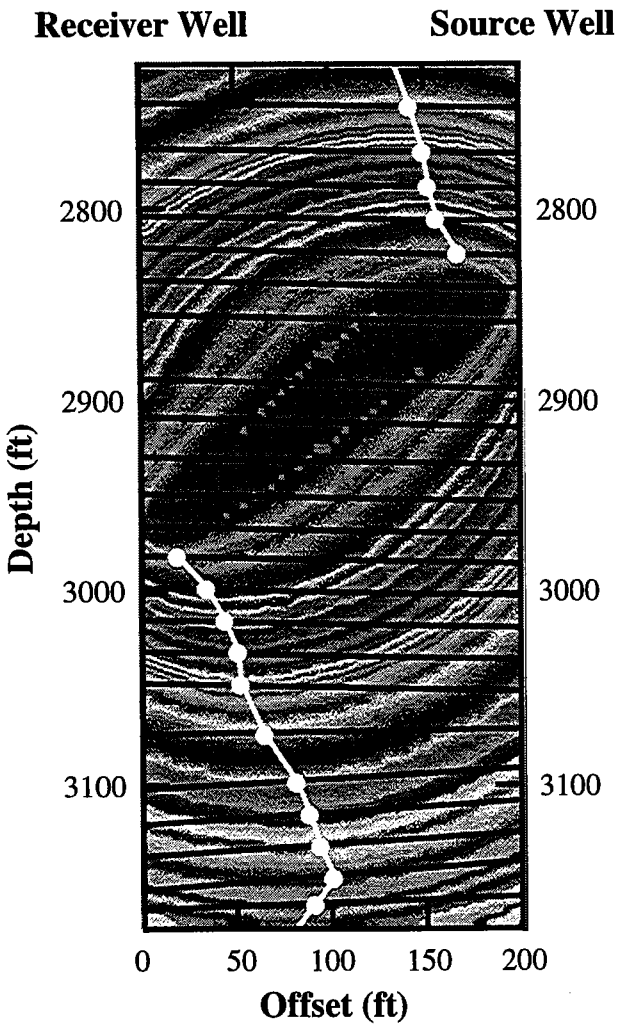

Figure 14: This figure illustrates how the reflector geometries shown in Fig. 11 are used with the combined traveltime map from Fig. 13 to obtain mapping trajectories in a general 2-D model. The reflection points are defined by shared points of tangency between the reflecting horizons and the combined traveltime map isochrons.

CALCULATING XSP-CDP TRAJECTORIES WITHOUT RAYTRACING

An approach for calculating XSP-CDP mapping trajectories without raytracing can be formulated as an extension of work done by Matsuoka and Ezaka (1992). Their work describes a method for calculating direct and once-reflected raypaths using the concepts of reciprocity and wavefronts. As described previously, reflection points occur where the tangent of an isochron of the combined traveltime map equals the tangent of the reflecting horizon. The difficulty of implementing this technique lies in determining these points. One criteria for identifying reflection points using isochrons of the combined traveltime map is that the reflection points correspond to stationary points of total traveltime along the reflecting interface. The validity of this can be proven using a geometrical argument or the weak formulation of Fermat's principle (Born and Wolf, 1980).

Reflection points are stationary points of traveltime

To show that reflection points correspond to stationary points of total traveltime along the reflecting interface using a geometrical argument I use a single reflector from the model shown in Fig. 10. This single reflector is shown in Figure 15. Figure 16 shows a close-up of the reflection point R_D, and the nearby isochrons. A fundamental assumption of the XSP-CDP transformation is that for any source-receiver combination there is at most one reflection point for each reflecting horizon. Under this assumption it can be seen that a reflecting horizon can be related to a combined traveltime isochron in only one of three ways: the reflecting horizon does not touch the isochron, the reflecting horizon crosses the isochron one or more times, or the reflecting horizon shares only one point, a point of tangency, with the isochron.

The gradient of a combined traveltime isochron is normal to its tangent in isotropic media. For a point to satisfy the conditions required of a reflection point under the Law of Reflections for wavefronts the tangent of the reflecting horizon and the tangent of the isochron must be equal at that point. Since the tangent of the combined traveltime isochron is normal to the gradient, the derivative of traveltime along the tangent must be zero. As the tangent of the reflecting horizon is equal to the tangent of the isochron at the reflection point the derivative of traveltime at the reflecting horizon must also be zero. Therefore the reflection point is a stationary point of traveltime on the reflecting horizon.

A reflection point can also be shown to be a stationary point using the weak formulation of Fermat's principle (Born and Wolf, 1980). A reflection point on a reflecting horizon lies along a path which connects the source and the receiver through the reflection point. Under

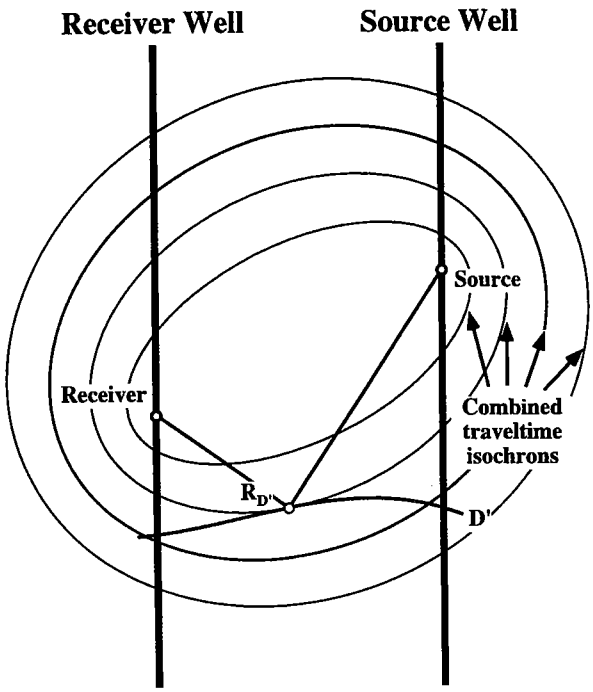

Figure 15: In this illustration the example shown previously in Fig. 10 has been simplified to include a single reflector, D', and the reflected raypath from a single source-receiver pair.

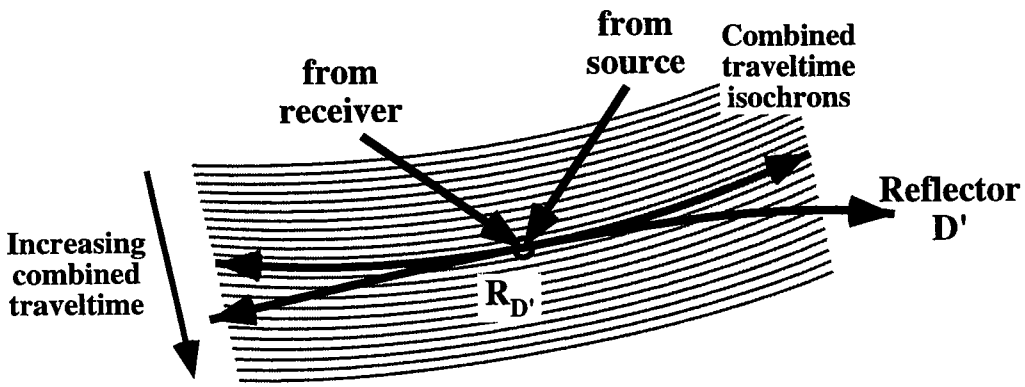

Figure 16: A close-up of the reflection point in Fig. 15. This figure illustrates graphically how the reflection point corresponds to a point where the combined traveltime along the reflecting horizon is stationary. In this case the stationary point is a traveltime minimum.

the weak formulation of Fermat's principle small perturbations of the location of the reflection point along the reflecting horizon *must*, to first order, result in *no* change to the total traveltime. This is a more fundamental proof of the stationarity of the traveltime at the reflection point since the reflection point is *defined* by the property of stationarity. More importantly, this proof also applies to anisotropic media whereas the geometrical proof is true only for isotropic media.

An efficient approach for calculating mapping trajectories

The property of stationarity of combined traveltime along the reflecting horizon allows a simple and straightforward approach for calculating mapping trajectories to be formulated. The flowchart for this procedure is shown in Figure 17. First, traveltime maps for all sources and receivers are precalculated using a model consisting of reflector geometries and a velocity model. Second, traveltime maps for the source and receiver of interest are added together to create the combined traveltime map. Third, the total traveltime for each point along a reflecting horizon is obtained from the combined traveltime map. Fourth, the point on the reflecting map where the traveltime is stationary is determined. This point corresponds to the reflection point and is one point on the mapping trajectory for that source-receiver combination. Reflection points for the remaining reflectors are determined sequentially until both the upgoing and downgoing mapping trajectories for the current source-receiver combination are defined. Finally, mapping trajectories for all source-receivers are determined sequentially resulting in mapping trajectories for the entire data set.

The efficiency of this approach results from the precalculation of all the source and receiver traveltime maps. When all source and receiver maps are precalculated the combined traveltime map for any source-receiver combination can be created quickly by simply reading and adding their precalculated maps. In this way the total number of maps required to determine all mapping trajectories is equal to the sum of the different source and receiver locations. After all traveltime maps are calculated the number of subsequent calculations is determined by the product of the number of source-receiver combinations and the number of reflecting horizons.

IMPLEMENTATION OF MAPPING ALGORITHM

The primary goal of my thesis work is to develop a consistent approach to the traveltime and reflection imaging of crosswell seismic surveys. Prerequisites for attaining this consistency are that the assumptions and parameterization of the model used in the traveltime and

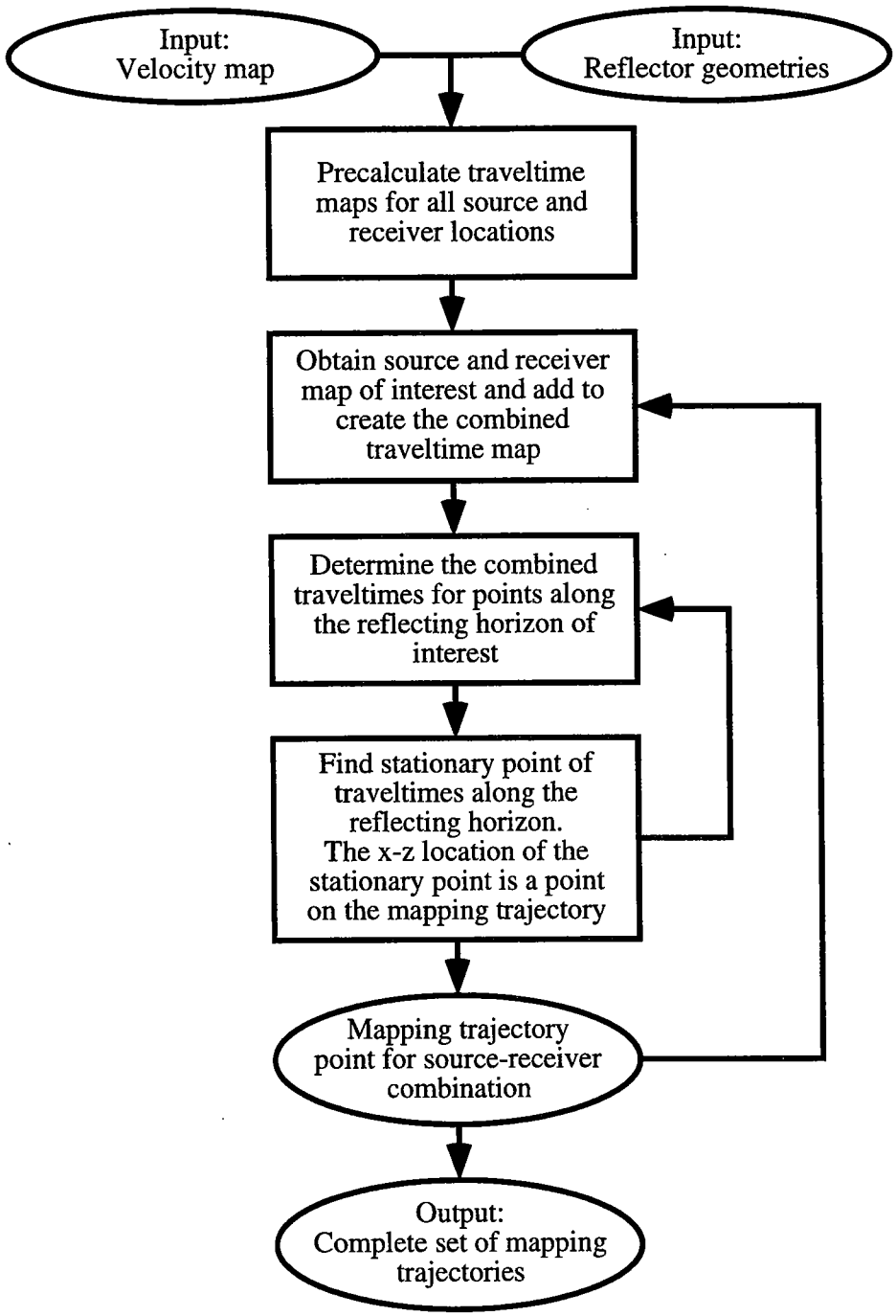

Figure 17: This flowchart illustrates the procedure for calculating mapping trajectories using the wavefront method of obtaining reflection points. The efficiency of this approach is obtained primarily through the precalculation of all the necessary source and receiver traveltime maps. This also allows trajectories to be calculated efficiently in any sort order, such as the Common Mid-Depth domain.

reflection imaging be the same. The determining factors which lead to the choice of one parameterization over another are encountered primarily in the traveltime tomography (Van Schaack, 1995a; Van Schaack, 1995b). The basic assumption used in my work is a ray-theoretic model. The parameterization of this model is one where a 2-D isotropic velocity field is defined by cells in offset-depth Cartesian coordinates. Reflectors are defined at points spaced equally across the image. Reflector locations intermediate to the defined points are calculated using cubic splines resulting in a smooth function in offset and depth. Well deviations are included by projecting the wells to a 2-D image space.

Calculating traveltime maps

The choice of a method for the calculation of the traveltime maps is an important decision in the implementation of the XSP-CDP mapping algorithm. Errors in the traveltime maps will propagate through the imaging steps resulting in a mispositioning of the mapped data. Fortunately, many accurate algorithms have been developed in recent years using a variety of different approaches. Two commonly used approaches are: finite-difference solutions of the eikonal equation (Vidale, 1988; Van Trier and Symes, 1991; Zhang, 1993) and methods based on Huygen's principle or graph theory (Saito, 1989; Moser, 1989).

Matsuoka and Ezaka (1992) described one advantage of using combined traveltime maps to calculate direct and reflected arrival raypaths as the ability of this approach to include head waves. Many methods of traveltime inversion use first breaks which may result from head waves. In the shooting method the paths of head waves cannot be calculated since an infinite number of head-wave paths exist for any given shooting angle. Figure 18 illustrates source and receiver maps computed using a model with a strong velocity contrast added to create the combined traveltime map. The head wave can be seen as an upward traveling linear event in both the source and receiver traveltime maps. In the combined traveltime map the first arrival raypath is defined by the minimum traveltimes, which in Fig. 18 result from a refracted head wave.

Unfortunately, the presence of head waves in the traveltime maps leads to errors in calculating the mapping trajectories. One problem is that, in the combined traveltime map approach, reflection points are defined by stationary points along reflecting horizons. The traveltimes along the segment of the head wave raypath lying along the interface are all equal. Since reflection points are defined as stationary points this contradicts the XSP-CDP mapping assumption that there is a unique reflection point on each reflector for each source-receiver pair. In essence, the reflection point cannot be correctly determined using the notion of stationarity of traveltimes in the presence of head waves. The second problem

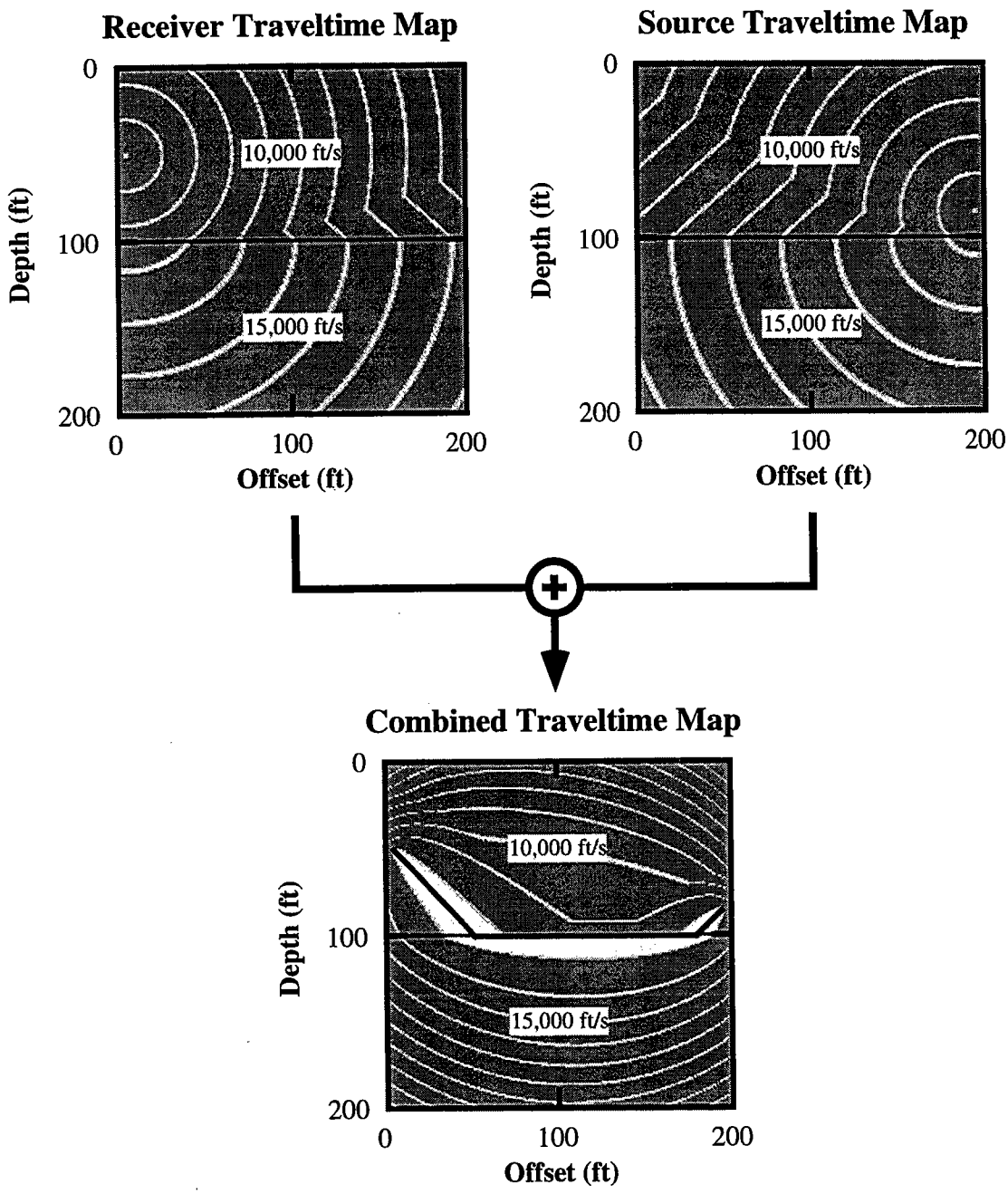

Figure 18: A combined traveltime map with dominant head waves. The source and receiver traveltime maps shown here were calculated using a Vidale-type finite-differences eikonal code (1988) which obtains first arrival traveltimes. The head wave in each traveltime map can be seen as an upward-traveling linear event. In this example the first, or fastest, arrival is a refracted head wave. The raypath for this event is defined by the minimum combined traveltime values.

is that even if the location of the reflection point can be identified the traveltime of the combined traveltime map corresponding to that location will be incorrect. The traveltime will be that of the head wave first arrival.

In practice head waves are not always a problem. The velocity models for reflection imaging used in my work are, in general, the result of a combined direct and reflected arrival traveltime inversion. The parameterization of the model and the smoothing constraints used in the inversion preclude the possibility of the large velocity contrasts required to create head waves. For this reason, virtually any accurate method for calculating traveltime maps will provide good results for many of the cases encountered. Nevertheless, it may be desirable to map data with a model which may include sharp velocity contrasts between layers. For this reason I have chosen to use a finite-differences eikonal code which calculates energetic arrivals.

The scheme I use to calculate traveltime maps is a derivative of an approach formulated by Mo (1994). Mo's approach is based on Vidale's (1988) finite-difference solution of the eikonal equation. The fundamental difference between the two codes is that Mo's approach allows wavefronts to be discontinuous across boundaries. This occurs at post-critical incidence. Figure 19 shows an example of Vidale's approach applied to the calculation of source, receiver, and combined traveltime maps. This example is similar to that shown in Fig. 18 except that both upgoing and downgoing head waves are present. Figure 20 shows the same traveltime maps calculated using Mo's method.

A comparison of Figs. 19 and 20 yields several interesting observations. In Fig. 19 the first arrival is a downgoing head wave from the interface at 100 ft. The first arrival in Fig. 20 is a direct arrival along the straight raypath connecting the source and receiver. Wavefronts created using Vidale's method are continuous while those resulting from Mo's method can be discontinuous across the interfaces. Finally, in this example, differences in the combined traveltime maps are confined to be within the slow layer; outside the slow zone the wavefronts are identical in Vidale's and Mo's method. So, using Mo's energetic-arrival eikonal scheme allows mapping trajectories to be calculated correctly in zones where head waves are present. Outside of these zones the results are identical to those that would be obtained using Vidale's finite-difference eikonal scheme.

In summary, there are a wide variety of methods to calculate traveltime maps. Much of the research in the area of developing these techniques has been directed toward increasing their efficiency and accuracy in complex velocity models. While all of these techniques offer their own advantages and disadvantages I have chosen to use Mo's energetic arrival approach to calculate traveltime maps for the following reasons:

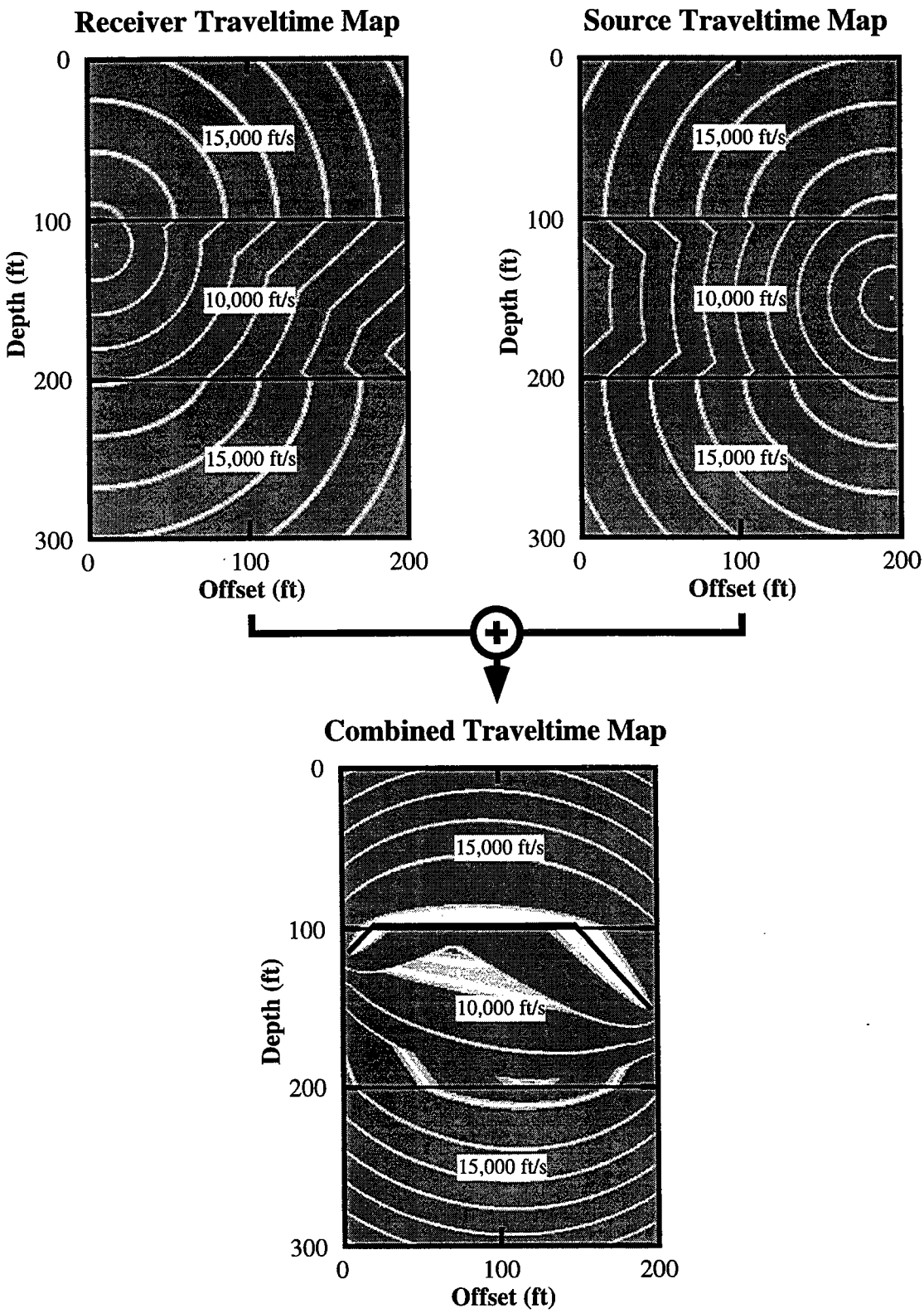

Figure 19: A second example of a combined traveltime map calculated from source and receiver maps which have strong head-wave events. In this case the head waves occur from velocity contrasts above and below the source and receiver positions.

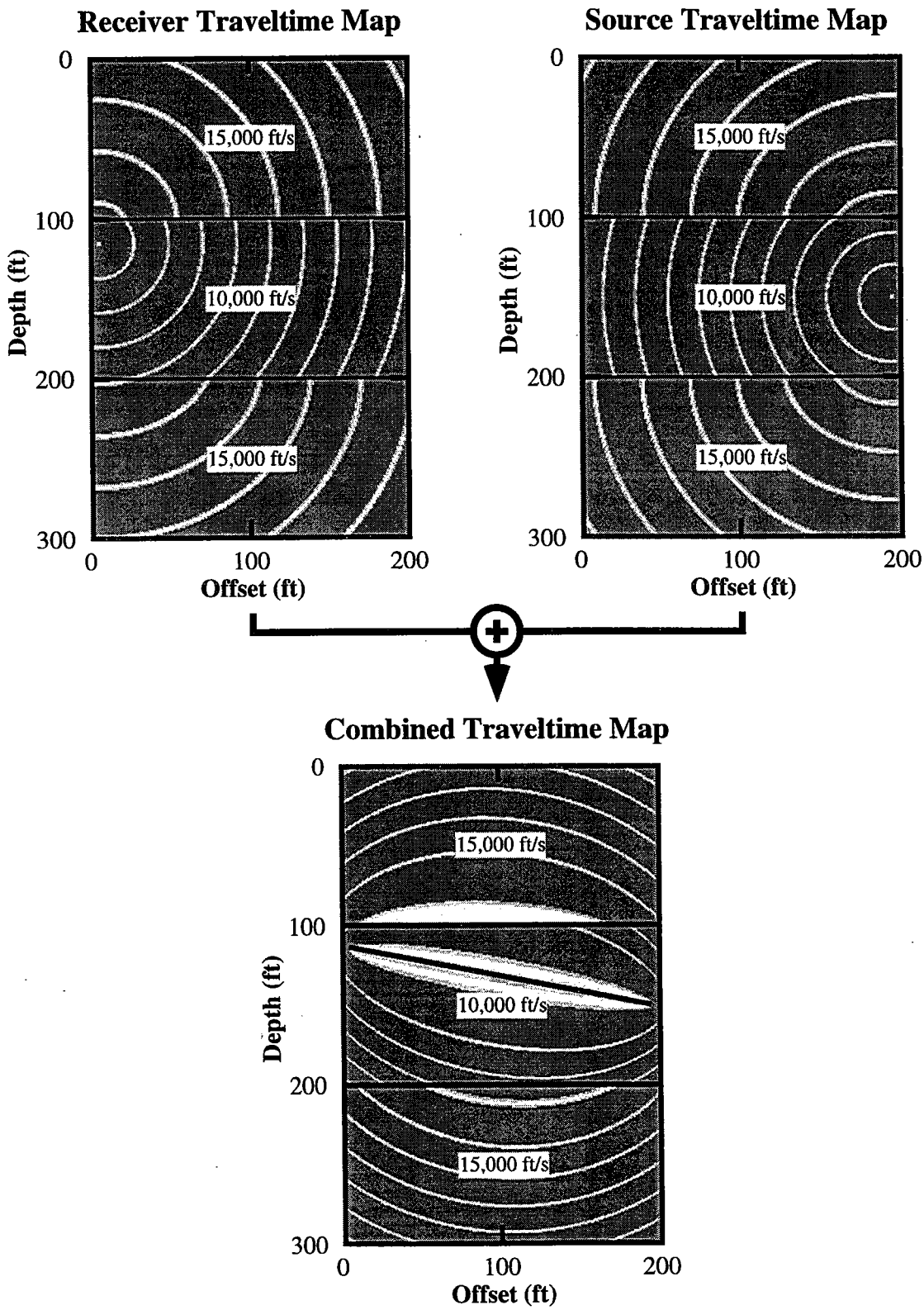

Figure 20: A combined traveltime map obtained through the use of an energetic-arrival finite-differences eikonal code (Mo, 1994). In this example head waves are removed effectively which will allow accurate mapping trajectories to be calculated.

- It incorporates the simplicity, efficiency and accuracy of Vidale's finite-differences eikonal code.
- It uses a cell model which is consistent with the cell model I use in the traveltime tomography.
- The effects of head waves are minimized.
- It can be easily modified to handle elliptical anisotropy with a vertical axis of symmetry.

With respect to future development, the ability to calculate mapping trajectories using the combined traveltime map approach is independent of the technique used to calculate the traveltime maps. Newer, faster, and more accurate techniques can therefore be incorporated easily as they are developed. As the model parameterization is modified to incorporate increasing complexity, anisotropy perhaps, XSP-CDP mapping can be accomplished in an identical fashion with only the calculation of the traveltime maps requiring modification.

Determining stationary points along the reflecting horizon

Once a combined traveltime map has been calculated for a source-receiver pair the final step in defining the mapping trajectories is to determine the reflection points for the reflecting horizons. As previously described, the reflection point on a reflecting interface is defined by the stationary point of combined traveltime. The reflection point is determined by locating the stationary point on each reflecting horizon. All reflection points for a source-receiver pair define the upgoing and downgoing mapping trajectories.

A schematic for the flow used to calculate the mapping trajectories for a single source-receiver pair is shown in Figure 21. The input data for this procedure are the combined traveltime map for the source and receiver of interest and a set of reflector geometries defining the reflector orientations over the zone covered by the combined traveltime map.

Reflectors are parameterized using a cubic spline representation. This parameterization forces the reflector to vary smoothly which is consistent with the ray-theoretic assumption used in the XSP-CDP mapping transformation. Each reflector is defined by a set of depth values which are evenly spaced across the imaged area. Figure 22 shows an example of an imaged area defined by the combined traveltime map and a single reflector. The combined traveltime map is represented by the grid of equally spaced vertical and horizontal grey lines. A combined traveltime value is defined at each intersection point of the grey grid lines. The wells fall within the imaged area and are defined by the source and receiver locations within the imaged area. The reflector is defined by a set of depth values equally spaced across the model. The location of the reflector in between these points is determined

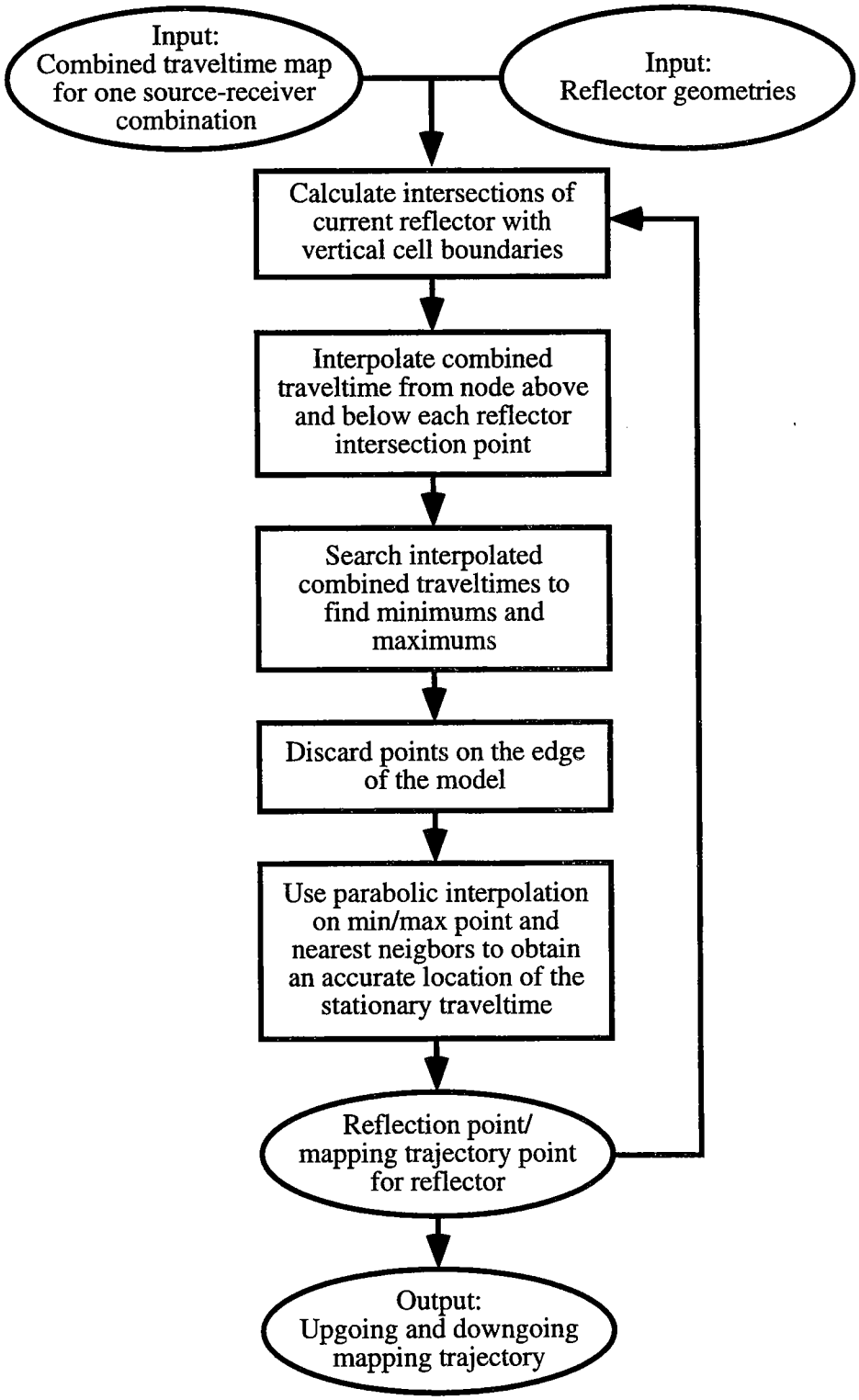

Figure 21: A flowchart describing the procedure for calculating the upgoing and downgoing mapping trajectories for a single source-receiver pair using the wavefront method.

using a cubic spline algorithm.

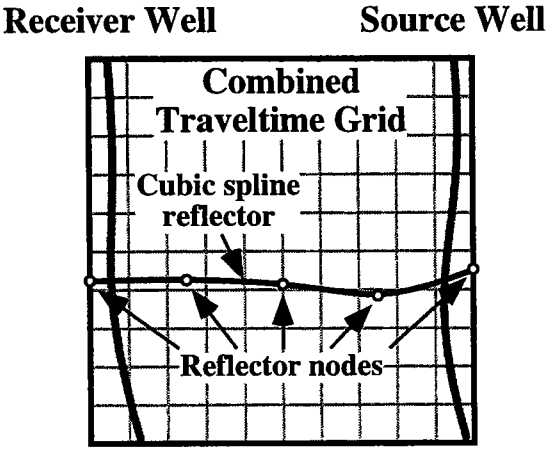

Figure 22: Reflectors are defined at points equally spaced across the image area. The reflector is interpolated between these point using cubic splines.

The next step in determining the reflection point is to obtain traveltimes along the extent of the reflecting horizon. The procedure used to accomplish this is to calculate the intersection of the reflector with the vertical node lines. The result of this calculation is illustrated in Figure 23. Once the intersection of the reflector with the vertical node lines is computed, traveltime values at the nearest nodes, above and below the intersection point, can be used to obtain an interpolated traveltime at the reflector. This procedure is used to define the combined traveltimes along the entire reflecting horizon. The problem of identifying the stationary point from these interpolated combined traveltimes is an exercise in

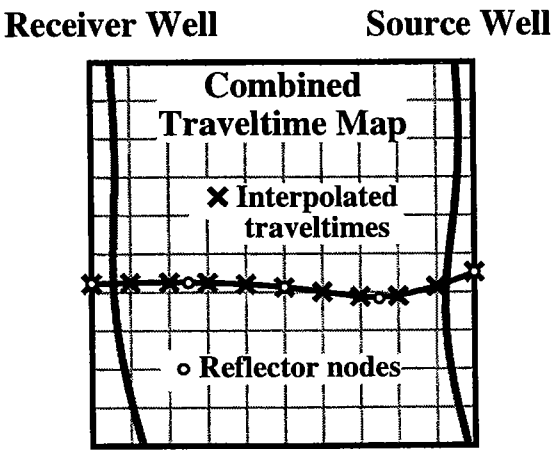

Figure 23: The reflector depth is determined for each vertical node using cubic splines so that combined traveltimes along the reflector can be defined through linear interpolation of the traveltime values above and below each interpolated reflector point.

locating the minimum and maximum values and determining which of these is truly stationary. One important note: if the XSP-CDP mapping assumption is valid, that there is at most one reflection point per reflecting interface, there should no more than one stationary point along the reflecting horizon. This requires that the stationary point be either the absolute minimum or absolute maximum combined traveltime.

Traveltime values at the left or right edge of the image may be minimum or maximum values of traveltime but they must be discarded since knowledge of the traveltimes past the edge must be used to determine whether they are actually stationary points. After the edge points have been discarded there should be, at most, one minimum or maximum point left. Since the location of this point is discretized by the vertical node line spacing it represents an estimate of the true location of the stationary point. If the spacing of nodes is fine this estimate may be adequate for mapping. I obtain a more precise estimate of the location of each stationary point using a parabolic interpolation scheme. The minimum/maximum traveltime and the adjacent traveltime values are used to define a parabola from which a more accurate estimate of the stationary point can be calculated. The final estimate of the stationary point represents the reflection point on the reflector which defines one point along either the upgoing or downgoing mapping trajectory.

EXAMPLES

The combined traveltime map approach for calculating mapping trajectories has been shown to be relatively simple in spite of the fact that it can be used to map 1-D through 2-D crosswell data with equal efficiency. In this section I provide examples of the wavefront approach for calculating mapping trajectories.

Calculating a mapping trajectory for a single source-receiver pair

This first example illustrates the computation of upgoing and downgoing mapping trajectories for the single source-receiver pair used in Fig. 14. Figure 14 is redisplayed in Figure 24 with the reflecting horizons labeled from top to bottom. Reflectors R_1 and R_{25} are at the top and bottom respectively of the image area defined by the combined traveltime map. The traveltimes on the combined traveltime map are defined every 5.0 ft in both the vertical and horizontal directions for a total image size of 41x91. In this example the reflecting horizons are linear, defined by the intersection depths with the sides of the image.

The flow diagram shown in Fig. 21 is used as a guide for the process of determining the mapping trajectories. For each reflector in turn, the intersection of the reflector with the ver-

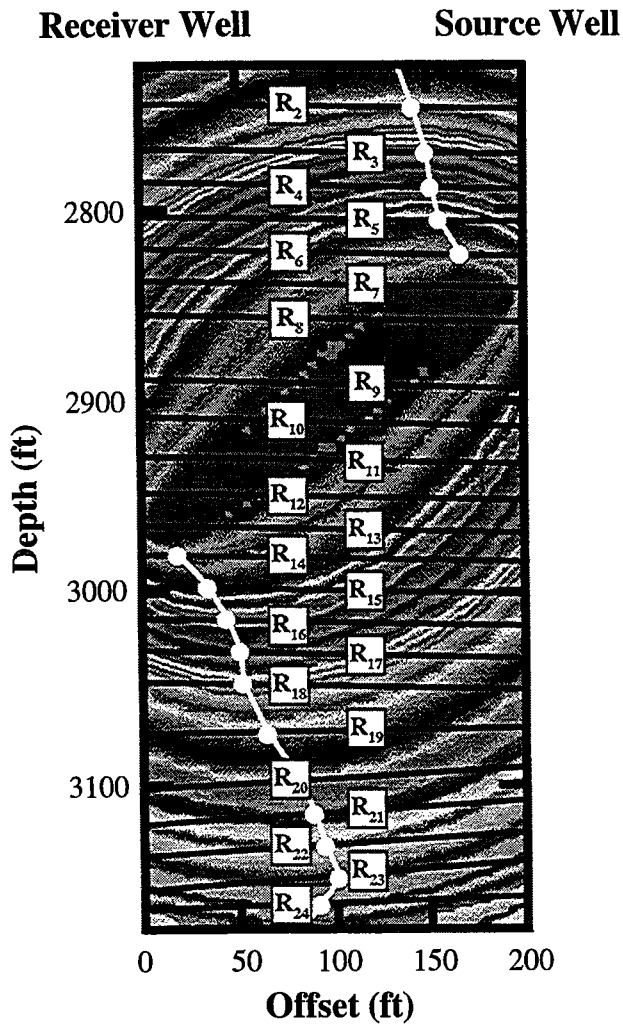

Figure 24: This figure illustrates how upgoing and downgoing mapping trajectories are calculated using the wavefront method for the single source-receiver combination previously shown in Fig. 2.13. Reflection points are defined for each reflecting horizon from top to bottom by locating the point of stationarity of combined traveltime along the individual reflector. These reflection points constitute points on the mapping trajectory. Mapping trajectory points intermediate to these are obtained by interpolation.

tical nodes is found, or in other words, the depth of the reflector every 5.0 ft across the image is determined. The depth of intersection of the reflector with the vertical nodes is used to interpolate between nearest vertical neighbors to find the combined traveltime at the reflector. The traveltimes are then searched to find the minimum and maximum traveltime values along the interface and the edge points are discarded. The stationary point is estimated from the remaining minimum or maximum traveltime using parabolic interpolation so that a lateral resolution of better than 5.0 ft can be achieved. The reflection point is recorded and the next reflecting horizon is considered.

Figures 25 and 26 show data used in the determination of the downgoing and upgoing mapping trajectories seen in Fig. 24. Interpolated combined traveltimes along each reflector are shown including the final interpolated value. Several important points can be seen in Figs. 25 and 26. First, a number of reflectors are omitted: specifically reflectors numbered 7–13. These reflectors lie vertically between the source and receiver locations so no reflections are possible. In spite of this, stationary points of combined traveltime may exist so they must be excluded prior to the search for reflection points. The second important point is that the stationary points are all traveltime minima for both upgoing and downgoing reflections. This is not true in general. If the curvature of the reflector exceeds the curvature of the combined traveltime isochron the stationary point of traveltime may be a traveltime maximum.

Mapping trajectories in different domains in complex media

This example illustrates the use of the wavefront method for calculating mapping trajectories in different domains. First it is useful to describe these domains and some advantages and disadvantages of using each for crosswell reflection imaging. Figure 27 shows pictorially the mapping trajectories in four commonly used domains: Common Shot Gather (CSG), Common Receiver Gather (CRG), Common Mid-Depth Gather (CMG), and the Common Offset Gather (COG). The model used to define the trajectories in this first case consists of a constant velocity with horizontal reflectors; these trajectories were calculated using the equations in Fig. 1. These gathers are equivalent to their surface seismic counterparts except the variable dimension is vertical not horizontal. For example, in a CMG the average of the source and receiver *depths* is constant.

Typically, ray shooting methods are most efficient at linking rays in either the CSG or CRG domains. This is because a single reference fan can be calculated initially and used to guide the process for linking a number of rays in each gather. In both the CMG and COG domains a new reference fan is required to calculate each ray since all source and receiver

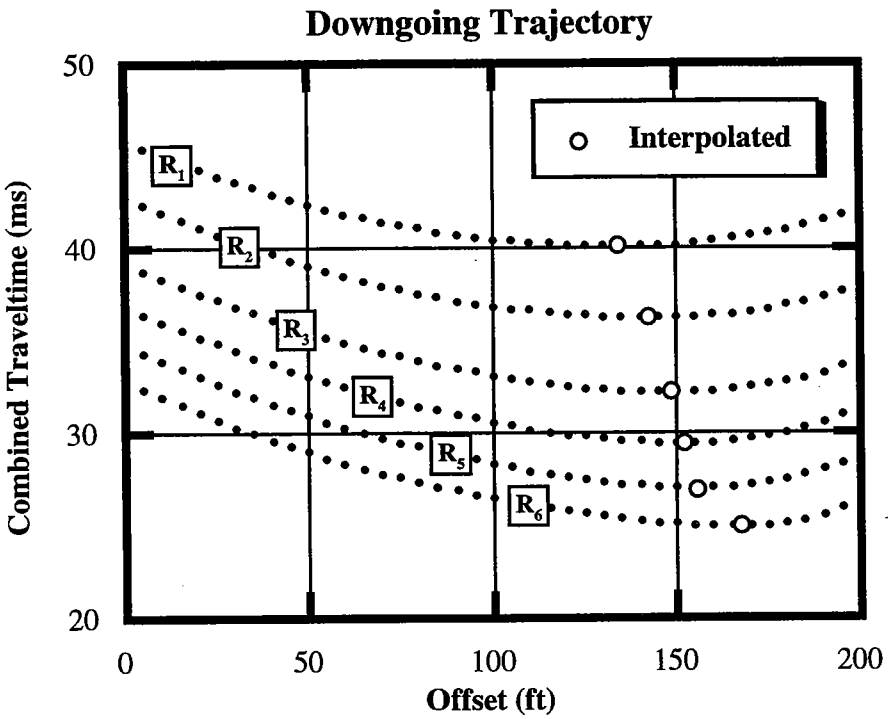

Figure 25: Combined traveltimes along each of the reflecting horizons leading to downgoing reflections. An accurate estimate of the stationary point of combined traveltime for each reflector is obtained using a parabolic interpolation routine.

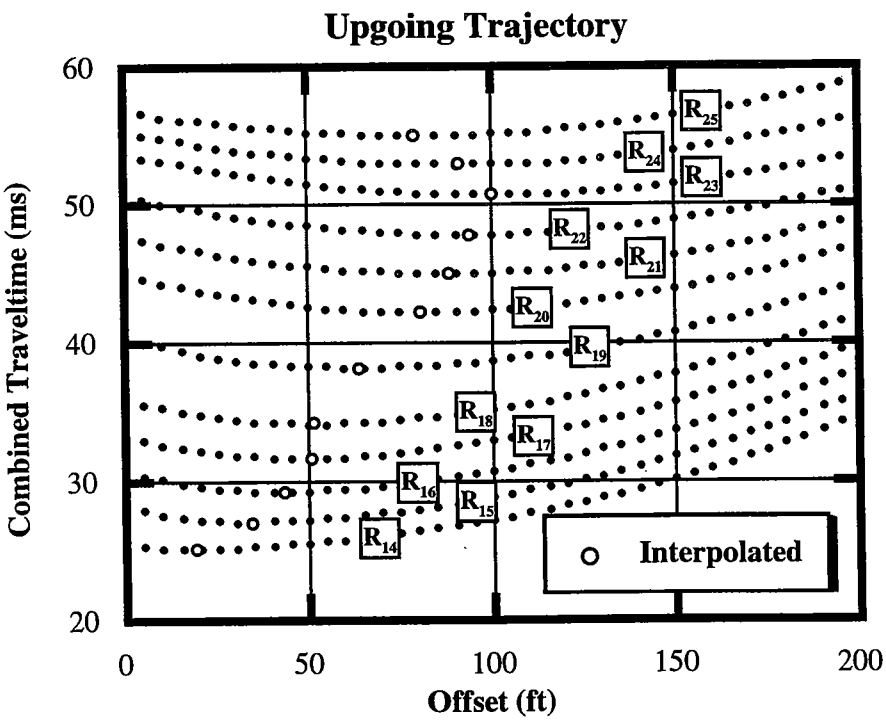

Figure 26: Combined traveltimes along each of the reflecting horizons leading to upgoing reflections and interpolated stationary points.

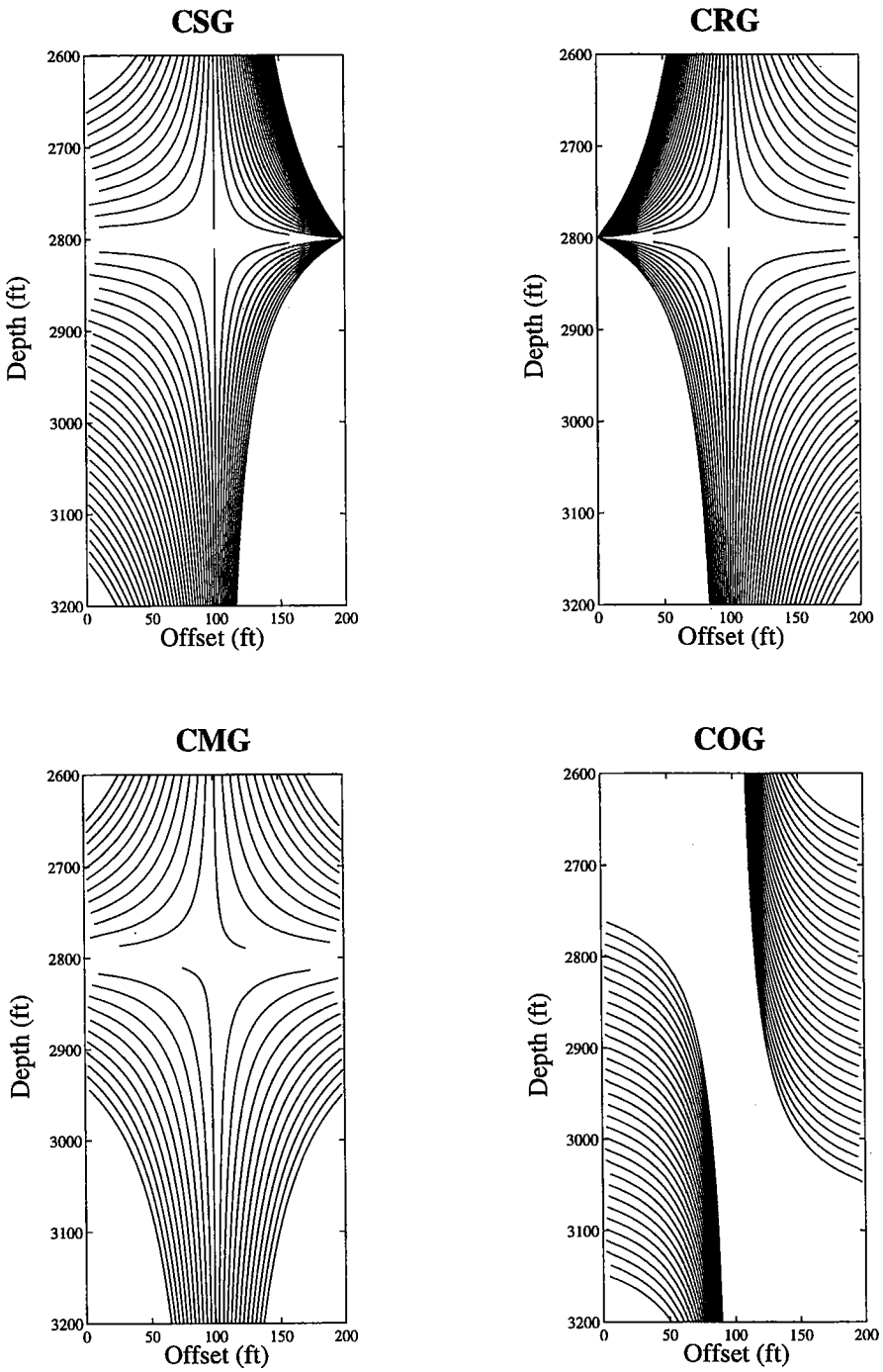

Figure 27: Mapping trajectories for crosswell seismic traces in 4 sort domains: common shot, common receiver, common mid-depth, and common offset. These trajectories are calculated from the equations shown in Fig. 1. As can be seen in this display, the CMG provides the most uniform coverage in the image space and the COG the least uniform. In a homogeneous model with flat reflectors, reflections at each depth would have the same angle of incidence for all trajectories in a mapped CMG. This results in a uniform wavelet at each depth

locations are unique in these gathers. This makes the CMG and COG data domains very inefficient for calculating trajectories using ray shooting methods so mapping trajectories are most commonly calculated in the CSG or CRG domains.

While the CSG and CRG domains may be more efficient for calculating the mapping trajectories there may be advantages to mapping in a less commonly used domain, the CMG domain. In spite of the fact that the sort type does not affect the individual mapping trajectories, or the total number of traces mapped, the different domains can have an effect on the accuracy of the interpolation used in the transformation step. The procedure for performing the data transformation, described previously, requires interpolation in both the vertical and horizontal directions to obtain evenly spaced data in the offset-depth image domain.

One advantage of the CMG is that the moveout of horizontal reflectors is minimized in the time-depth data domain, and the transformed wavelet is nearly stationary in depth in the offset-depth image domain (Lazaratos, 1993). This suggests that horizontal interpolation will be more accurate in the CMG because the stretching of the wavelet is almost constant at each depth. Also, as can be seen in Fig. 27, the CMG provides the most uniform spacing of mapping trajectories at each depth. This minimizes the aliasing of steeply dipping events. And, while steeply dipping events can still be aliased in the CMG domain, the dip at which events become aliased is constant across the image for each depth making it easier to avoid.

The orthogonal sort to the CMG, the COG, appears to have fewer benefits with respect to mapping. As can be seen in Fig. 27 the COG mapping trajectories are unevenly spaced at each depth. This can lead to aliasing of dipping events which occurs as a function of offset within the image. In addition, the wavelet is not stationary at each depth which can reduce the potential accuracy of the interpolation step. Finally, the upgoing and downgoing images overlap in depth. While upgoing and downgoing data are typically separated before mapping, a single mapped gather covers a much more restricted portion of the image domain as compared to the other domains.

One advantage of the wavefront mapping method is that it can be used to calculate mapping trajectories in any of the previously described domains directly. Since the traveltime maps are precalculated and stored in memory the order in which the different source-receiver mapping trajectories are calculated does not affect the program efficiency. Since the computation time is not affected significantly by the sort domain the optimum imaging domain can be used in every case with no penalty.

Figure 28 shows mapping trajectories in the same domains calculated using the wavefront method and the 2-D velocity and reflector model shown in Fig. 11. The mapping tra-

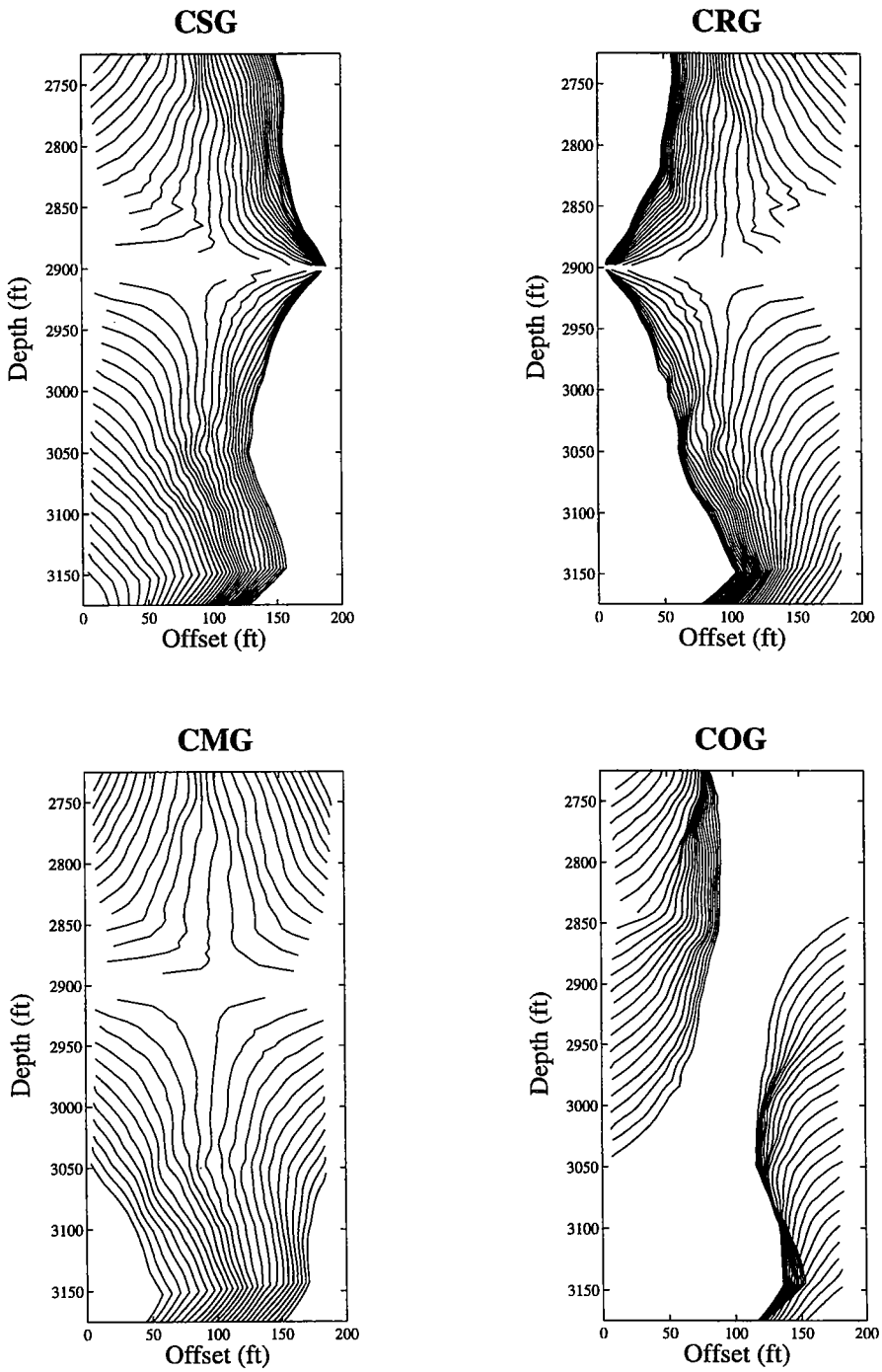

Figure 28: Mapping trajectories in different domains obtained using the wavefront method. These trajectories were calculated using the 2-D velocity model and reflector geometries shown previously in Fig. 11. Compare these trajectories to the equivalent trajectories for a homogeneous model and flat reflectors shown in Fig. 27.

jectories shown in Fig. 28 have the same basic characteristics as those shown in Fig. 27. The effect of the 2-D velocity model and dipping interfaces is reflected in the distortion of the mapping trajectories in all of the domains. The COG trajectories show the undesirable trait of overlapping each other in the bottom right-hand portion of the image area. This overlapping, effectively, results in some stacking of the data during the transformation. This precludes the possibility of optimal processing prior to stacking. The CMG data domain still exhibits the desirable property of spacing the trajectories in the most uniform manner throughout the image area.

McElroy *S*-wave field example

In this example field data are mapped using the velocity and reflector geometry results of a CDRATT inversion (Van Schaack, 1995b). These inversion results were introduced earlier in this paper and can be seen in Fig. 11. The focus of this example is on the optimal stacking of the mapped data.

The processed upgoing and downgoing data were mapped independently with the wavefront-based method from the CMG domain. Following the mapping these gathers were transformed to the Angle Versus Amplitude (AVA) domain (Lazaratos, 1993). This domain was introduced by Lazaratos as a tool to help monitor and edit the range of incidence angles over which useful reflections could be stacked. Figure 29 illustrates this transformation graphically. The data are originally mapped gather by gather into the offset-depth image domain as shown in Fig. 29a. Following the completion of the mapping the data are sorted into constant offset (offset versus mid-depth) gathers. Mid-depth is then transformed into a local angle of incidence using a straight ray approximation to provide the final offset versus angle of incidence gathers (named by Lazaratos "AVA" gathers) as shown in Fig. 29b.

Prior to mapping, the McElroy *S*-wave data were processed to create two data sets, one with enhanced upgoing reflections and the other with enhanced downgoing reflections. Figures 30 and 31 show selected AVA gathers from these mapped upgoing and downgoing data. Each figure consists of four AVA gathers taken at 25, 75, 125, and 175 ft from the 200 ft image. As is suggested in Fig. 29, each of these gathers is summed, or stacked, to create a single trace in the reflection image.

Information necessary to optimize the stacked image is easily obtained from the AVA gathers. The basic information required is the range of incidence angles for which the traces in the AVA are stacked. Ideally this choice should include the widest range of incidence angles which satisfy these three criteria: the range of incidence angles is relatively uniform

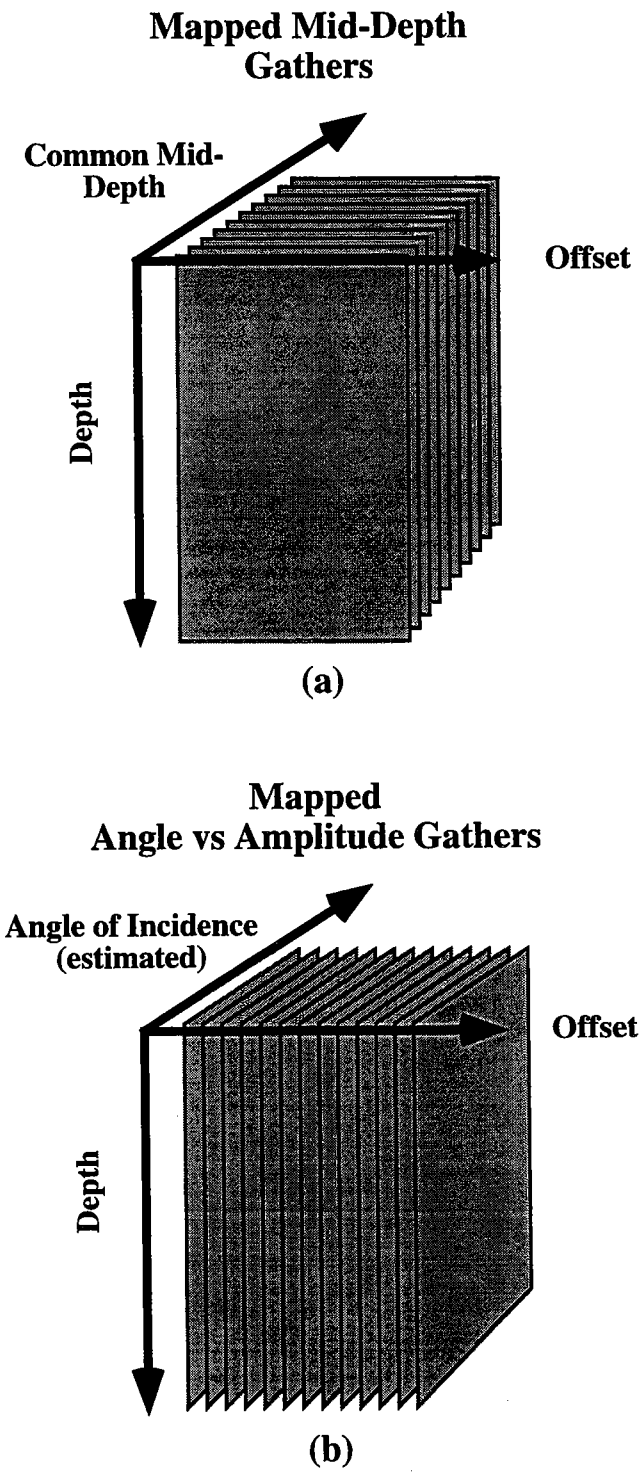

Figure 29: This figure illustrates graphically the transformation of XSP-CDP mapped data from the offset-depth domain, shown in (a) above, to the Angle versus Amplitude (AVA) domain, shown in (b). Each AVA gathers consists of a single offset for which the mapped data are transformed to reflect the angle of incidence. The transformation used in this work to convert data to angle of incidence employs a straight ray approximation.

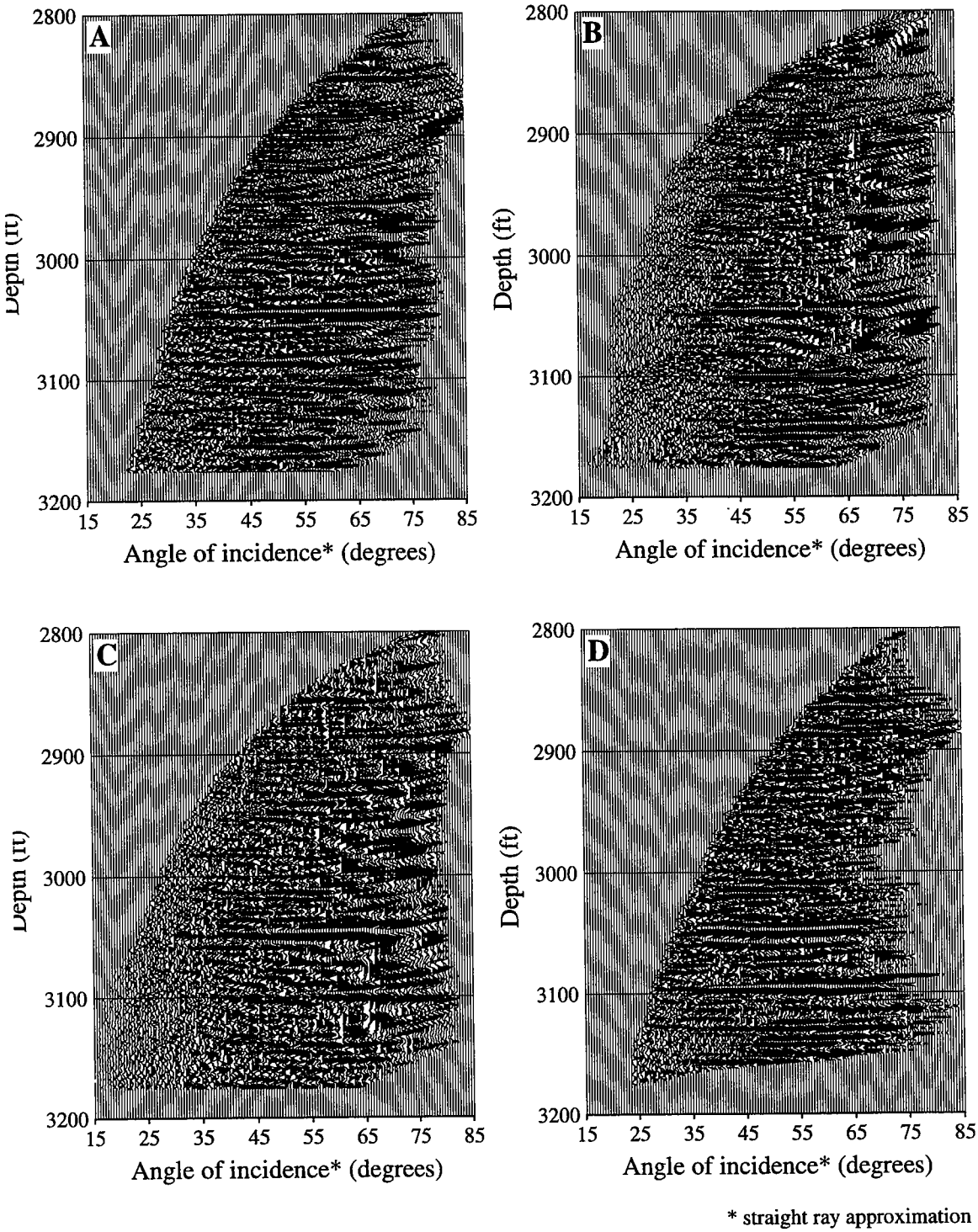

Figure 30: The AVA gathers shown above are for offsets sampled evenly across the 200 ft image space at 25, 75, 125, and 175ft, images a–d respectively. These gathers are created from data processed and mapped to image upgoing reflections.

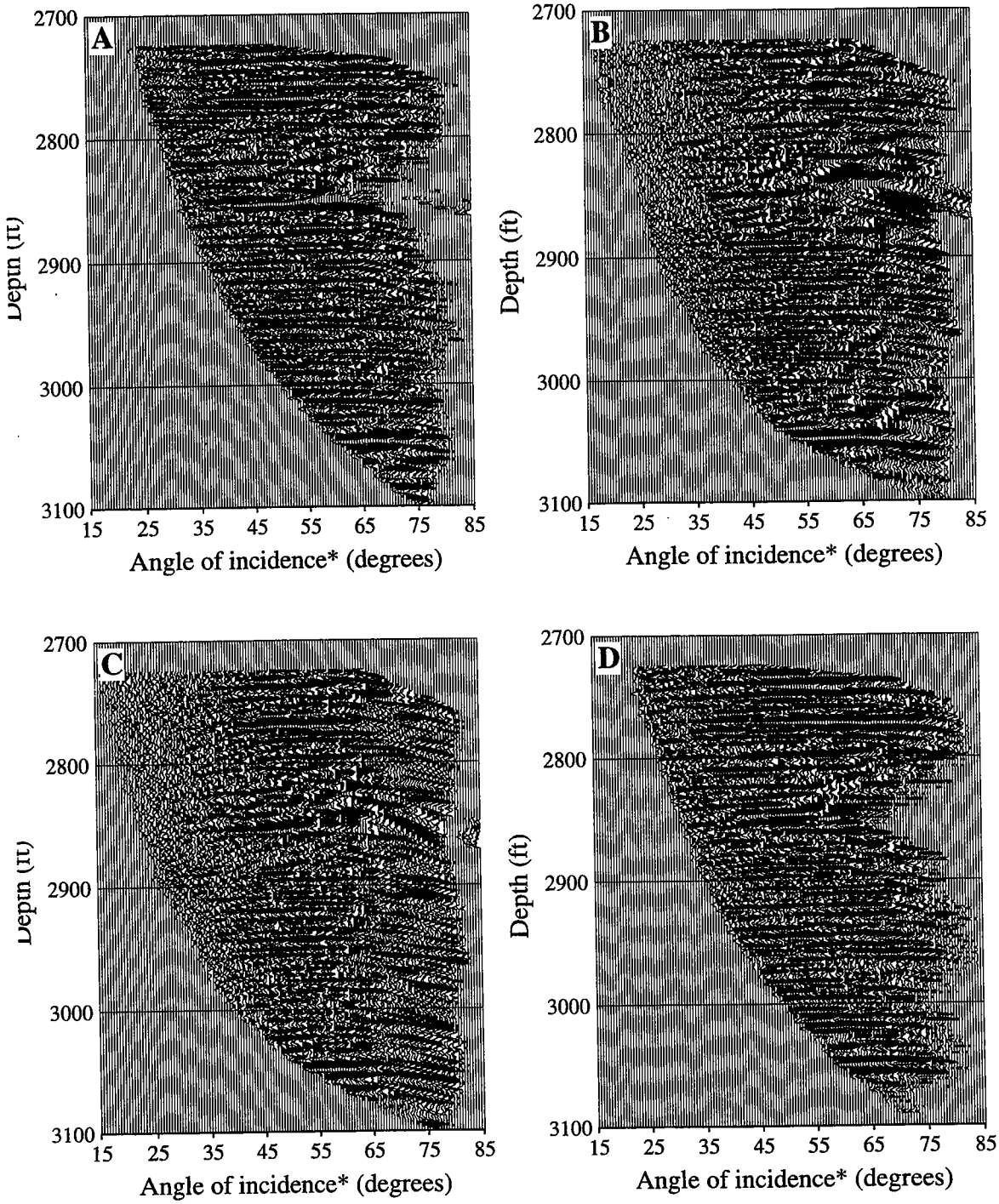

Figure 31: The AVA gathers shown above are for offsets sampled evenly across the 200 ft image space at 25, 75, 125, and 175ft, images a–d respectively. These gathers are created from data processed and mapped to image downgoing reflections.

within the trace, the reflection events are flat, and good signal-to-noise ratio. These criteria are crucial to image quality. Figure 32 provides an example of a stacked image where the entire range of incidence angles is stacked without discrimination.

While the upgoing and downgoing stacks shown in Fig. 32 contain much of the high resolution seen in previous images of these data (Lazaratos, 1993), stacking quality can be improved upon by removing data which does not contribute constructively to the final image. It can be seen in the AVA gathers shown in Figs. 30 & 31 that the highest data quality is present between the angles of 35–65 degrees. Reflections with an angle of incidence less than 35 degrees exhibit a poor signal-to-noise ratio, particularly for AVA gathers near the center of the image. Reflections with angles of incidence larger than 65 degrees exhibit a great deal of stretch and line up poorly with the same reflected events with more moderate angles of incidence. Also, by limiting the range of angles stacked from 35-65 degrees, each trace will contain a more uniform wavelet from top to bottom.

Figure 33 shows the results of stacking a narrower range of angles. A general improvement in the quality of the reflections can be seen in these new stacks, particularly in the upgoing stack above 3050 ft. While the improvements are noticeable they are not as dramatic as might be expected. This suggests that the stacking procedure is effective in minimizing the effects of the poor signal-to-noise and stretched data. Another possibility for improving the stack quality lies in avoiding any undesirable effects that may have occurred in the reflection enhancement step.

Figures 34 and 35 show AVA gathers at the same offsets as in Figs. 30 and 31 with the difference that the data mapped in this case were not processed to enhance upgoing or downgoing reflections. In other words, the raw field data was mapped directly. It can be seen that the unprocessed data contain a large amount of noise. In spite of this, coherent reflection events are still obvious in these gathers. This suggests that reasonable reflection images might be obtained in this case simply by mapping and stacking the raw data. In Figure 36 the results of this experiment are presented. The data have been stacked for a range of incidence angles 35–65 degrees, identical to the reflection images shown in Fig. 33.

The reflection images from the stacked raw data exhibit several interesting characteristics. One point which is immediately obvious is that the general structure of these new images is essentially the same as that seen in the images shown in Fig. 33. This provides a welcome reassurance that these structures are not merely processing artifacts. The fact that accurate images can be created directly from the raw data given an appropriate mapping model hints at the importance of these models.

A second observation is that while some noise can be seen in the new images they appear to contain a significant amount of high frequency information which seems to have

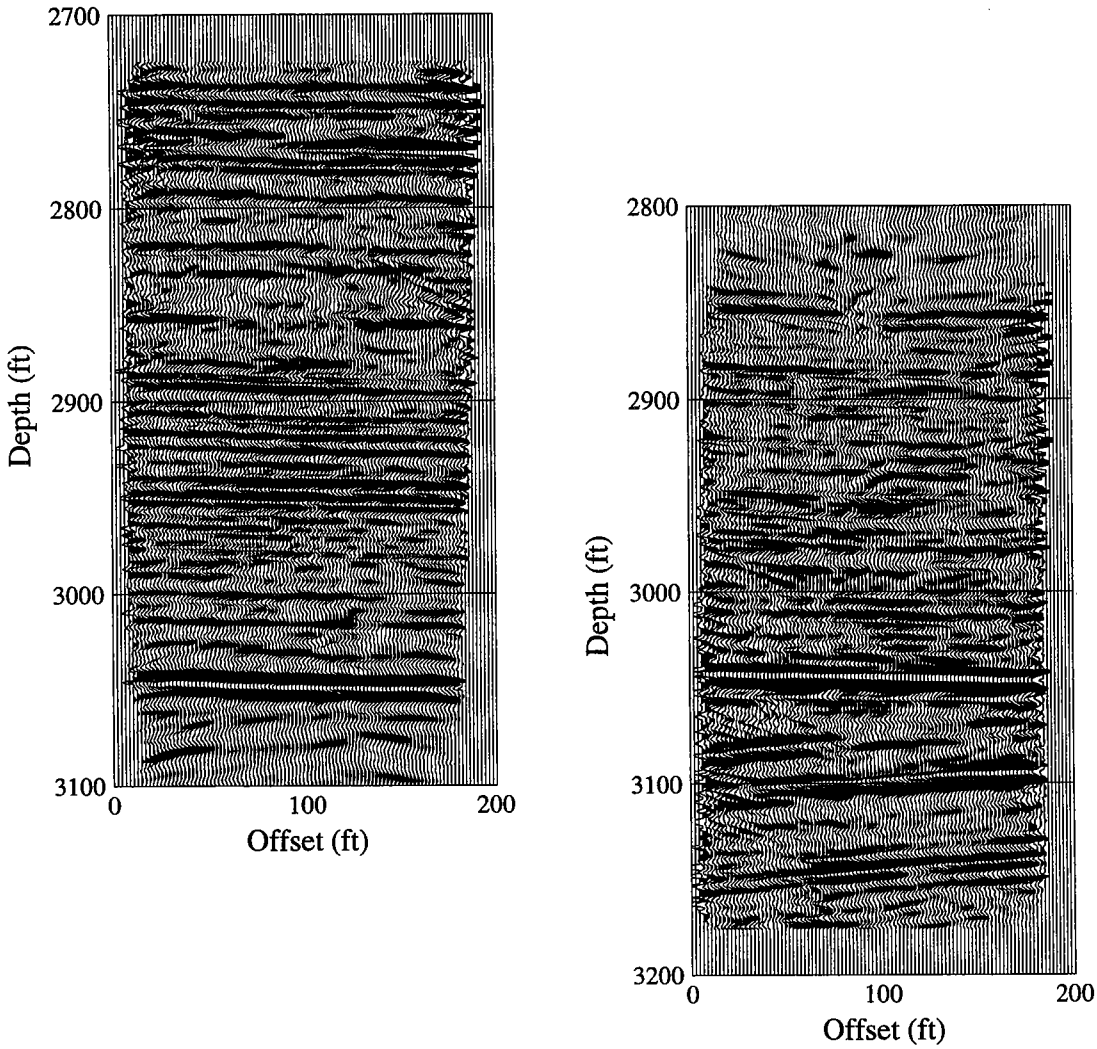

Figure 32: These upgoing and downgoing *S*-wave images are obtained by stacking AVA gathers, including those shown in Figs. 30 & 31, over the entire range of incident angles. Downgoing reflections are shown in the left-hand-side image and upgoing reflections are shown in the right-hand-side image. An angular unconformity can be seen clearly in the upgoing reflection image at about 3050 ft.

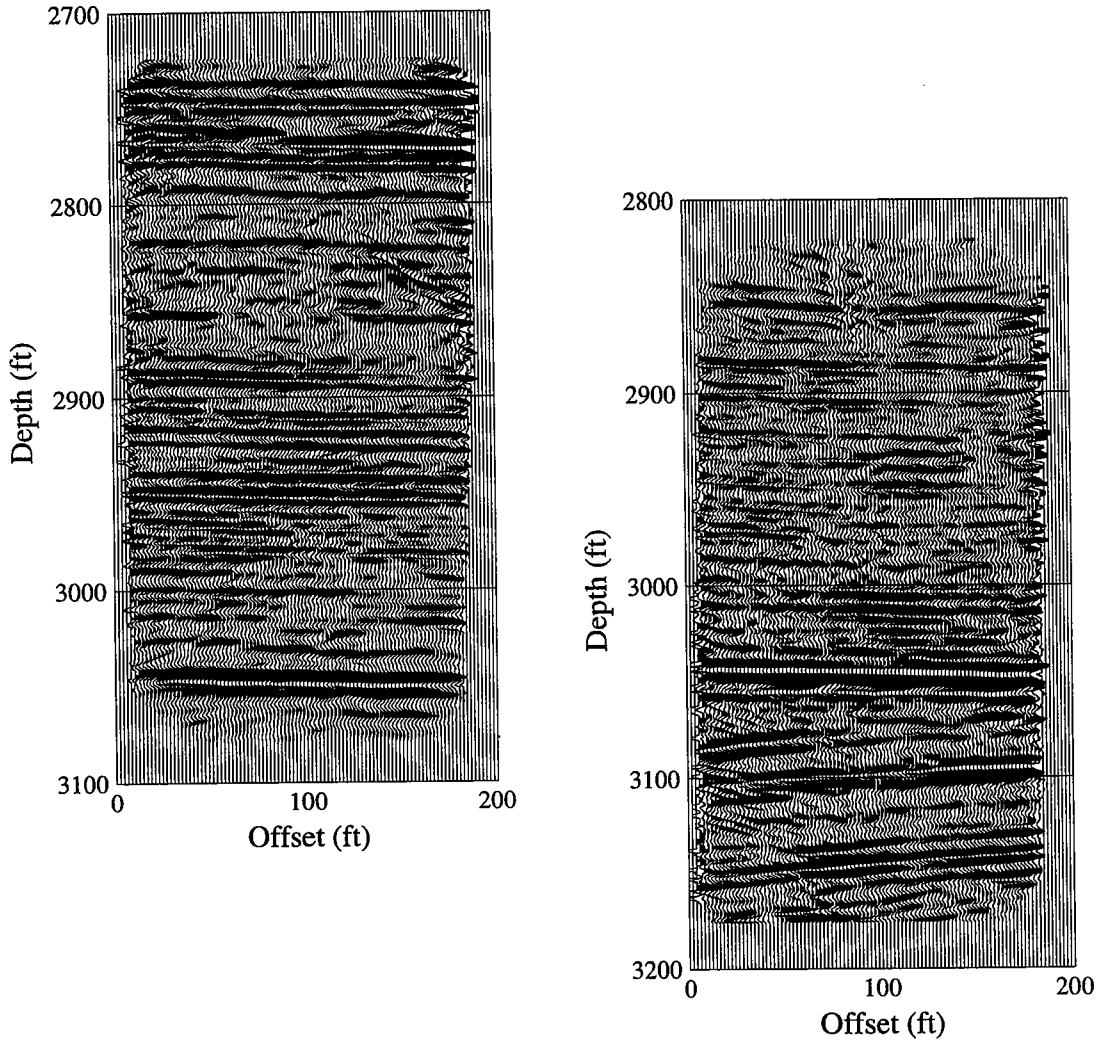

Figure 33: These upgoing and downgoing *S*-wave reflection images are obtained by stacking AVA gathers, including those shown in Figs. 30 & 31, using only incident angles from 35–65 degrees. A small reduction in noise and improvement in overall coherency can be seen when compared to the reflection images shown in Fig. 32.

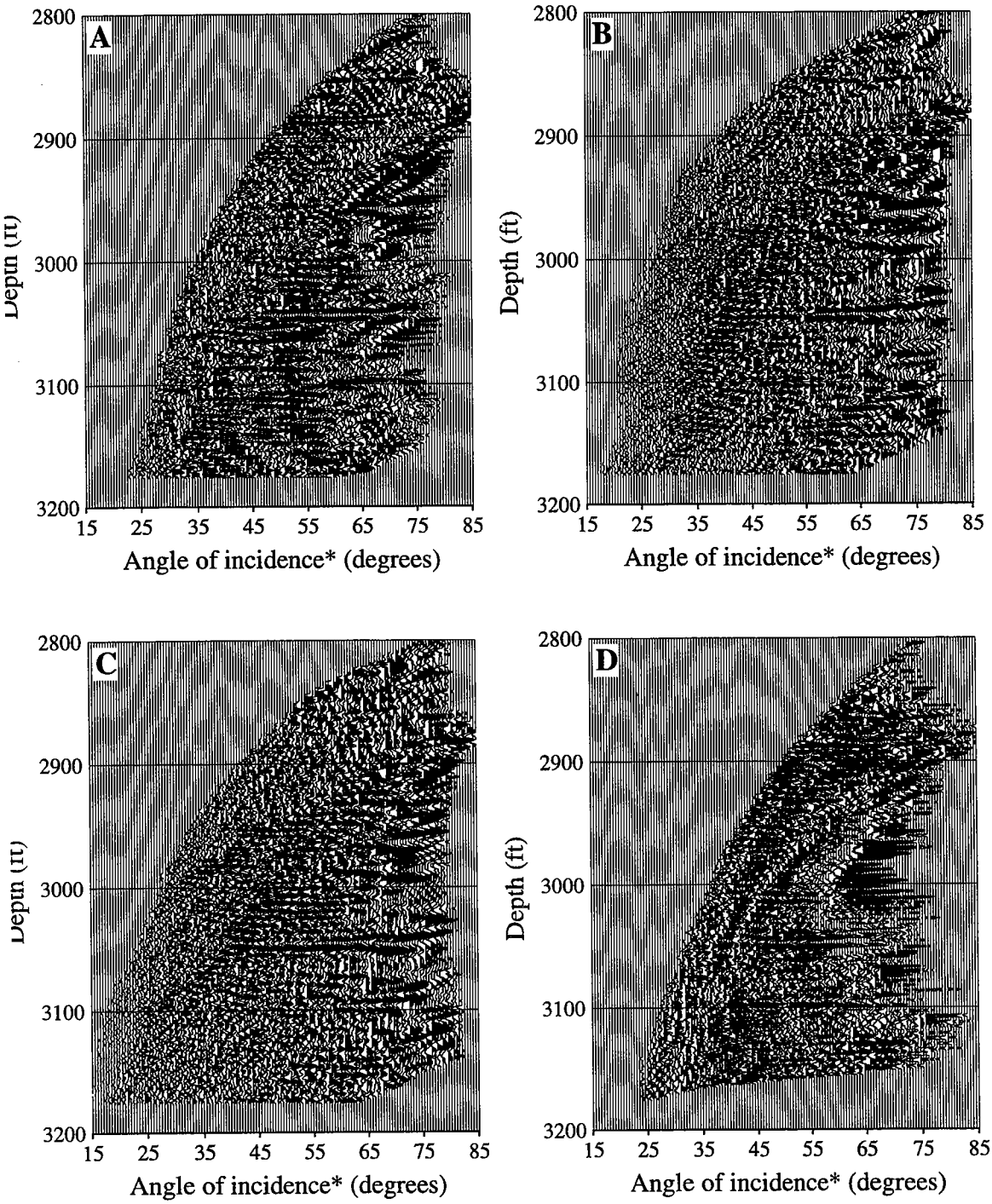

Figure 34: The AVA gathers shown above are for offsets sampled evenly across the 200 ft image space at 25, 75, 125, and 175ft, identical to those offsets shown in Figs. 30 & 31. The difference in these gathers is that the data used to create them has not undergone any wavefield separation or reflection enhancement. These gathers are mapped to image upgoing reflections.

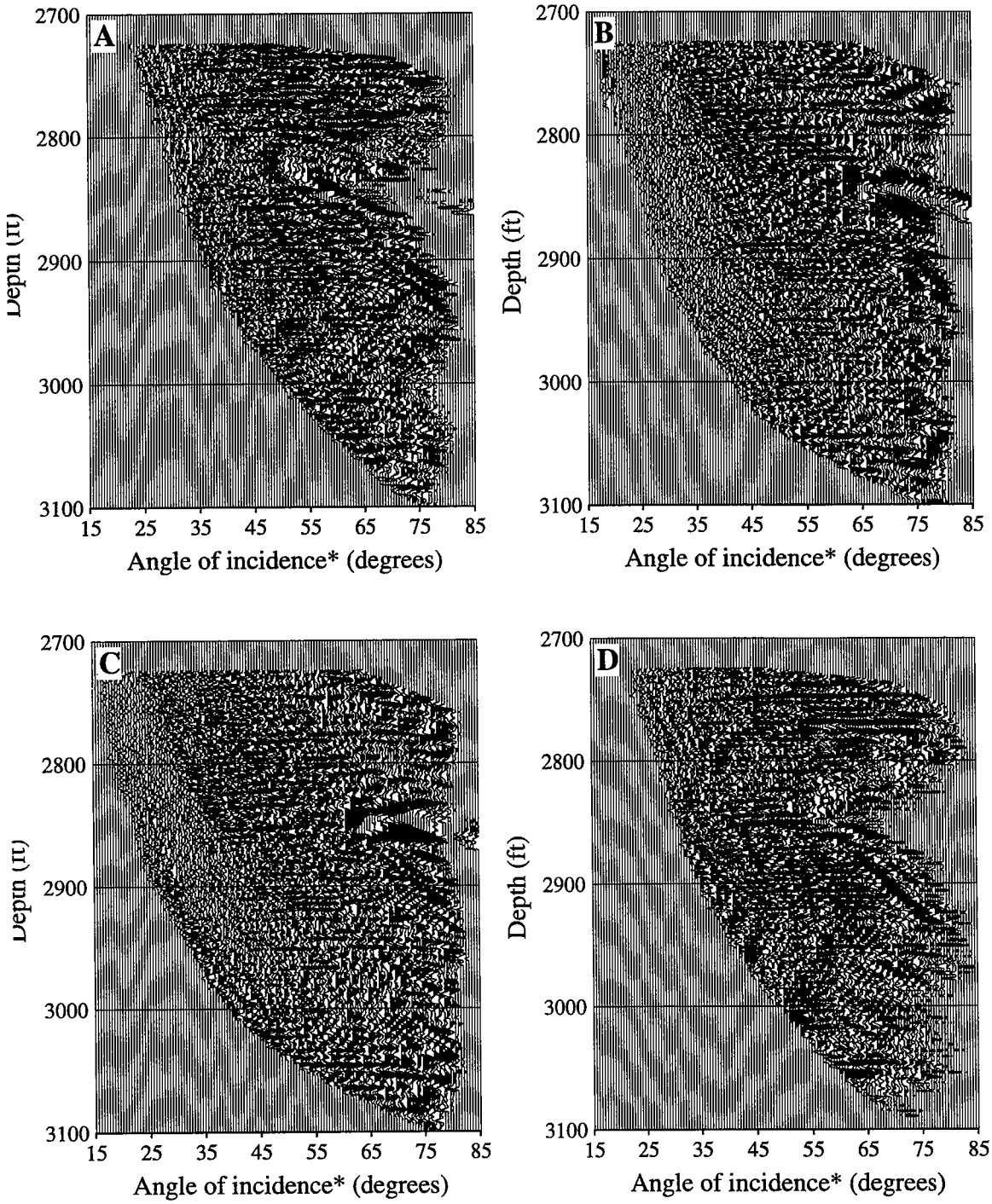

Figure 35: The AVA gathers shown above are for offsets sampled evenly across the 200 ft image space at 25, 75, 125, and 175ft, identical to those offsets shown in Figs. 30 & 31. The difference in these gathers is that the data used to create them has not undergone any wavefield separation or reflection enhancement. These gathers are mapped to image downgoing reflections.

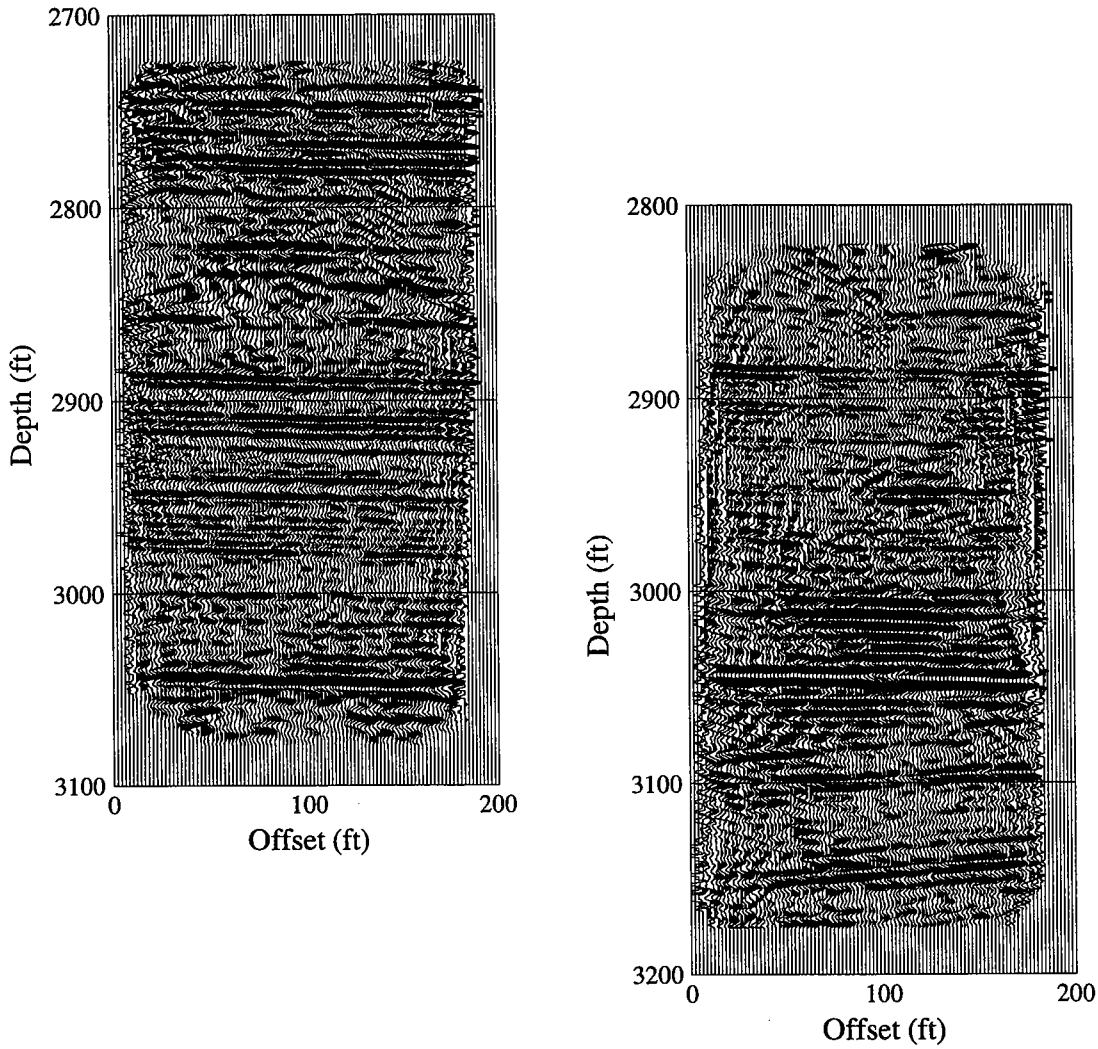

Figure 36: The upgoing and downgoing *S*-wave reflection images shown above are obtained by stacking AVA gathers, including those shown in Figs. 34 & 35, using only incident angles from 35–65 degrees. The data used to create these images have undergone *no* preprocessing. In other words, these reflections images are made directly from the raw seismic data. While some coherent noise exists which is not present in the reflection images shown in Fig. 33, these images contain more high frequency information. This example illustrates the power of stacking when the appropriate mapping model is used.

been lost in the reflection enhancement processing done to create the images shown in Fig. 33. This suggests that wavefield enhancement and separation techniques must be carefully applied to maintain optimal image resolution. While the reflection enhancement process applied to the data used to create the reflection images shown in Fig. 33 has removed a number of noise events present in the images shown in Fig. 36 it appears to have been at the expense of some of the high frequencies present in the data. On the other hand it was only through this enhancement process that reflections were made pickable for traveltimes. This was necessary to perform the CDRATT inversion which provided the velocity model and reflector geometries used to map the data. Clearly wavefield processing/reflection enhancement is a key component to acquiring the accurate mapping model necessary for optimal reflection imaging.

While the focus of this paper is on XSP-CDP mapping in complex models without raytracing, the success of this field example shows the usefulness of providing a consistent approach for velocity and reflection imaging. This success also provides evidence supporting the use of ray-theoretic approaches for crosswell imaging, at least under the conditions in which this experiment was conducted.

CONCLUSIONS

In this paper I have introduced a new method for calculating XSP-CDP mapping trajectories without the use of raytracing. The implementation of the method described in this paper is designed to use as an input model a 2-D isotropic velocity field defined by constant velocity cells and reflectors defined using cubic splines. The choice of this parameterization for the XSP-CDP mapping model was determined by a criterion of consistency with the combined direct and reflected arrival traveltime tomography described in previous work (Van Schaaack, 1995a; Van Schaaack, 1995b).

Calculating mapping trajectories using the combined traveltime approach is relatively simple. Upgoing and downgoing mapping trajectories are calculated in two basic steps. First traveltime maps are calculated for all source and receiver locations. In the second step mapping trajectories are determined by adding the appropriate source and receiver traveltime maps and then locating reflecting points on each interface. The reflecting point on each interface coincides with the stationary point of total traveltime along the interface. Since the traveltime maps are precalculated mapping trajectories can be determined for source and receiver combinations in any order without any loss of efficiency.

Traveltime maps are calculated in the implementation described in this paper using an energetic arrival finite-difference eikonal code. This minimizes the distortion of the map-

ping trajectories due to head waves in models which have strong velocity contrasts. One important feature of the combined traveltime approach for calculating mapping trajectories is that the method can be extended easily to more complex models such as those incorporating anisotropy. The only aspect of the method that needs to be modified to handle more complex models is the algorithm for calculating traveltime maps. The calculation of the mapping trajectories and the data transformation are independent of the traveltime map calculations.

The field example shown in this paper illustrates the effectiveness of the CDRATT inversion for obtaining a mapping model and the XSP-CDP mapping algorithm presented here for mapping with this model. High resolution reflection images can be made using this consistent approach even when the mapped data are not processed to enhance reflections. This provides a welcome reassurance that reflections imaged in the crosswell experiment are not simply artifacts of the wavefield processing steps.

References

Abdalla, A. A. and Stewart, R. R., 1990, Traveltime inversion and reflection processing of cross-hole seismic data: 60th Ann. Internat. Mtg. of SEG., Expanded Abstracts, 47–50.

Baker, L. J. and Harris, J. M., 1984, Cross-borehole seismic imaging: 54th Ann. Internat. Mtg. of SEG., Expanded Abstracts, 23–25.

Beydoun, W. B., Delvaux, J., Mendes, M., Noual, G., and Tarantola, A., 1989, Practical aspects of an elastic migration/inversion of crosshole data for reservoir characterization: A Paris basin example: Geophysics, **54**, 1587–1595.

Born, M. and Wolf, E., 1980, Principle of optics electromagnetic theory of propagation interference and diffraction of light, 6th Edition, Pergamon Press, Inc., 808.

Delvaux, J., Nicoletis, L., Noual, G., and Dutzer, J. F., 1987, Acquisition techniques in cross-hole seismic surveys: 62nd Ann. Tech. Conf. and Expos. of SPE., Proc. no. 16785, 23–25.

Dillon, P. B. and Thomson, R. C., 1984, Offset source VSP surveys and their image reconstruction: Geophys. Prosp., **32**, 790–811.

Findlay, M. J., Goulty, N. R., and Kragh, K. E., 1991, The crosshole seismic reflection method in opencast coal exploration: First Break, **9**, 509–514.

Goulty, N. R., Thatcher, J. S., Findlay, M. J., Kragh, J. E., Jackson, P. D., 1990, Experimental investigation of crosshole seismic techniques for shallow coal exploration: Quarterly Journal of Engineering Geology, London, **23**, 217–228.

Hu, L.-Z., McMechan, G. A., and Harris, J. M., 1988, Acoustic modeling and migration of stacked cross-hole data: Geophysics, **53**, 1015–1023.

Iverson, W. P., 1988, Crosswell logging for acoustic impedance: J. Pet. Tech., **40**, 75–82.

Lazaratos, S. K., 1993, Cross-well reflection imaging, Ph.D. Thesis, Stanford University.

Lazaratos, S. K., Harris, J. M., Rector, J. W., and Van Schaack, M. A., 1995, High-resolution crosswell imaging of a wet Texas Carbonate reservoir: Part 4 – Reflection imaging: Geophysics, **60**, 702–711.

Matsuoka, T. and Ezaka, T., 1992, Ray tracing using reciprocity: Geophysics, **57**, 326–333.

Mo, L.-W. and Harris, J. M., 1993, Migration of crosswell seismic data: field data case: STP-**4**, Paper L.

Mo, L.-W., 1994, Calculation of direct arrival traveltimes by the eikonal equation: STP-**5**, Paper K.

Moser, T. J., 1989, Efficient seismic ray tracing using graph theory: 59th Ann. Internat. Mtg. of SEG., Expanded Abstracts, 1106–1108.

Qin, F. and Schuster, G. T., 1993, Constrained Kirchhoff migration of cross-well seismic

data: 63rd Ann. Internat. Mtg. of SEG., Expanded Abstracts, 99–102.

Rowbotham, P. S. and Goulty, N. R., 1993, Imaging capability of cross-hole seismic reflection surveys: Geophys. Prosp., **41**, 927–941.

Saito, H., 1989, Traveltimes and raypaths of first arrival seismic waves: Computation method based on Huygen's principle: 59th Ann. Internat. Mtg. of SEG., Expanded Abstracts, 244–247

Smalley, N. and Harris, J. M., 1992, CDP stacking and imaging of cross-well reflectors: 62nd Ann. Internat. Mtg. of SEG., Expanded Abstracts, 87–90.

Tura, M. A. C., Greaves, R. J., and Beydoun, W. B., 1994, Crosswell seismic reflection/ diffraction tomography: A reservoir characterization application: Geophysics, **59**, 351–361.

Van Schaack, M. A., 1995a, Crosswell traveltime tomography using direct and reflected arrivals: Part 1 – Theory and implementation: STP-**6**, Paper G.

Van Schaack, M. A., 1995b, Crosswell traveltime tomography using direct and reflected arrivals: Part 1 – Examples: STP-**6**, Paper H.

Van Trier, J. and Symes, W. W., 1991, Upwind finite-difference calculation of traveltimes: Geophysics, **56**, 812–821.

Vidale, J. E., 1988, Finite-difference calculation of traveltimes: Bull. Seis. Soc. Am., **78**, 2062–2076.

Wyatt, K. D. and Wyatt, S. B., 1981, Determination of subsurface structural information using the vertical seismic profile: 51st Ann. Internat. Mtg. of SEG., Expanded Abstracts, 55–56.

Zhang, L., 1993, Imaging by the wavefront propagation method, Ph.D. Thesis, Stanford University.

Zhu, X. and McMechan, G. A., 1988, Acoustic modeling and migration of stacked cross-hole data: Geophysics, **53**, 492–500.